

ANALYSIS OF RESONANT ULTRASOUND SPECTROSCOPY AS A TECHNIQUE
TO EVALUATE MATERIAL PROPERTY CHANGES

A Thesis
presented to
the Faculty of the Graduate School
at the University of Missouri-Columbia

In Partial Fulfillment
of the Requirements for the Degree
Master of Arts

by
GAUTHAM MANOHARAN
Dr. Gary Solbrekken, Thesis Supervisor
MAY 2017

The Undersigned, appointed by the Dean of the Graduate School,
have examined the thesis entitled

ANALYSIS OF RESONANT ULTRASOUND SPECTROSCOPY AS A TECHNIQUE
TO EVALUATE MATERIAL PROPERTY CHANGES

presented by Gautham Manoharan,
a candidate for the degree for Master of Science,
and hereby certify that, in their opinion, it is worthy of acceptance.

Professor Gary Solbrekken

Professor Robert Winholtz

Professor Stephen Montgomery Smith

ACKNOWLEDGEMENTS

Firstly, I would like to thank my thesis adviser Dr. Gary Solbrekken for giving me the opportunity to work under him. He enabled a perfect learning atmosphere, taught me everything I needed to know about research and prepared me for challenges I might face in an industry environment.

I would also like to thank Nick Gazis from the European Spallation Source for his interest in this field which was the scope for my research. His valuable input helped me map out the direction I had to take my research.

Next, I would like to thank Abu Rafi Mohammed Iasir, whose previous work was the foundation for my entire research. His expertise in the area was more than helpful at times when I was stuck. I would also like to thank my lab colleagues, Jerome Rivers, Gerhard Schnieders, Han Han and Annemarie Hoyer who tolerated me as I worked away till late hours in the laboratory and aided with simulations and such.

Last but not least, I would like to thank my family and friends who were more than supportive of me throughout my research. Without them, it would have been a much tougher endeavor than it should have been.

TABLE OF CONTENTS

ACKNOWLEDGEMENTS	II
LIST OF FIGURES	VI
LIST OF TABLES	XI
NOMENCLATURE.....	XII
ABSTRACT.....	XIV
CHAPTER 1 – INTRODUCTION	1
1.1 Introduction.....	1
CHAPTER 2 – LITERATURE REVIEW	4
2.1 Effects of radiation.....	4
2.2 Resonant Ultrasound Spectroscopy.....	9
CHAPTER 3 – RUS: EXPERIMENTAL SETUP	11
3.1 Setup.....	11
3.2 Procedure.....	13

3.3 Data processing	16
CHAPTER 4 – FINITE ELEMENT METHOD: ABAQUS SIMULATION.....	19
4.1 Simulation procedure	19
4.1.1 Parameters/Variables.....	21
4.1.2 Parametric study.....	22
CHAPTER 5 – RESULTS AND ANALYSIS.....	23
5.1 Repeatability of the experiment.....	23
5.2 ABAQUS simulation results: Mesh study and constraints	27
5.2.1 Mesh type	28
5.2.2 Constraints on the model.....	31
5.2.3 Mesh fineness	34
5.3 ABAQUS simulation: Parametric study results.....	37
5.4 Experimental frequency response results vs simulation results	41
CHAPTER 6 – CONCLUSIONS AND FUTURE WORK	50
6.1 Conclusions.....	50
6.2 Future work.....	51
REFERENCES.....	53

APPENDIX A	57
Python code for parametric study	57
APPENDIX B	58
APPENDIX C	59
MATLAB code for obtaining parametric study trend graphs	59
APPENDIX D	60
MATLAB code for creating simple graphs of simulation results.....	60
APPENDIX E	61
APPENDIX F	63
APPENDIX G.....	67

LIST OF FIGURES

FIGURE 1.1: PARTICLE IRRADIATION IN ACCELERATORS 1

FIGURE 2.1: N_{DPA} FOR 2.6 MEV PROTONS AT FLUENCE OF 1017 P/CM² FOR ZIRCONIUM, CALCULATED USING SRIM 2003 CODE..... 5

FIGURE 2.2: NEUTRON DAMAGE 6

FIGURE 2.3: SWELLING% ($\Delta\rho/\rho$) OBSERVED IN PURE NICKEL IRRADIATED IN BOR-60 REACTOR (SQUARES) AND BN-350 (TRIANGLE AT 500°C ONLY) VS. IRRADIATION TEMPERATURE. DPA (DISPLACEMENTS PER ATOM) LEVELS ARE INDICATED FOR EACH DATA POINT..... 6

FIGURE 2.4: FRACTIONAL CHANGE IN YOUNG’S MODULUS OF 99.99 % COPPER AS A FUNCTION OF EXPOSURE TO 1-MEV ELECTRONS [11]. THE THREE DIFFERENT LINES ARE FOR THREE DIFFERENT SPECIMENS BASED ON HEAT TREATMENT: A WAS SLIGHTLY COLD WORKED, B WAS ANNEALED AND C WAS HEAVILY COLD WORKED..... 7

FIGURE 2.5: NANO-HARDNESS (A) AND YOUNG’S MODULUS (B) OF ZY-4 AND H-ZY SAMPLES BEFORE AND AFTER 2.6 MEV PROTON IRRADIATION..... 8

FIGURE 3.1: RUS TWO-PIN SETUP FOR SMALL SAMPLES 11

FIGURE 3.2: RUS THREE-PIN SETUP FOR LARGER SAMPLES	12
FIGURE 3.3: RUS EXPERIMENT DATA ACQUISITION.....	13
FIGURE 3.4: AMPLITUDE (VRMS IN V, M REPRESENTING X10-3) VS FREQUENCY (HZ). HERE THE RANGE CONSIDERED IS FROM 0 HZ TO 500 KHZ. THE PEAKS REPRESENT THE NATURAL FREQUENCIES OF THE SAMPLE.....	15
FIGURE 3.5: PHASE(DEGREES) VS FREQUENCY(HZ) FOR AN AL PARALLELEPIPED (DIMENSIONS 5 MM X 5 MM X 8 MM) IN THE FREQUENCY RANGE 100 KHZ TO 500 KHZ	16
FIGURE 3.6: FITSPECTRA GUI IN MATLAB WITH A DATA FILE FROM THE RESULTS OF NIOBIUM PARALLELEPIPED LOADED IN	17
FIGURE 3.7: Q FACTOR MEASUREMENT. $Q = F/\Delta F$.....	18
FIGURE 3.8: ADJUSTED CURVE FIT WHICH SAVES THE FREQUENCY AND Q FACTOR INFORMATION OF THE PEAKS.	18
FIGURE 4.1: FLOWCHART EXPLAINING THE INVERSE PROBLEM OF RU19	
FIGURE 5.1: REPRESENTATION OF THE FORWARD MODEL AND THE INVERSE PROBLEM IN RUS	23

FIGURE 5.2: FREQUENCY RESPONSE OF NIOBIUM RECTANGULAR PARALLELEPIPED (0HZ – 500KHZ) WITH 2000 DATA POINTS ON X-AXIS. FOR (A) AND (B) THE OUTPUT AMPLITUDE CHOSEN WAS 10V WHEREAS FOR (C) IT WAS 1V 24

FIGURE 5.3: FREQUENCY RESPONSE OF NIOBIUM THICK DISC (10MM DIAMETER, 3.2MM THICKNESS) IN FREQUENCY RANGE OF 0HZ-500KHZ WITH 2000 DATA POINTS ON THE X-AXIS. OUTPUT AMPLITUDE CHOSEN IS 0.1V FOR ALL THREE TRIALS 25

FIGURE 5.4: FREQUENCY RESPONSE OF NIOBIUM THIN DISC (10MM DIAMETER, 1MM THICKNESS) IN FREQUENCY RANGE OF 0HZ-500KHZ WITH 2000 DATA POINTS ON THE X-AXIS. OUTPUT AMPLITUDE CHOSEN IS 0.1V FOR ALL THREE TRIALS 26

FIGURE 5.5: PART GEOMETRY CONSTRUCTED IN THE ABAQUS GUI 28

FIGURE 5.6: MODE SHAPES FOR MODE NUMBERS 21 AND 25, AND THE CORRESPONDING NATURAL FREQUENCIES WHILE USING C3D8 ELEMENT TYPE..... 29

FIGURE 5.7: MODE SHAPES FOR MODE NUMBERS 21 AND 25, AND THE CORRESPONDING NATURAL FREQUENCIES WHILE USING C3D8R ELEMENT TYPE..... 30

FIGURE 5.8: LOW FREQUENCY MODES (CIRCLED) FOR STEEL HEX NUT (B), NB RECTANGULAR PARALLELEPIPED (C), AND NB THIN DISC (D). AL PARALLELEPIPED RESULTS (A) ARE SHOWN TO PROVE THAT THE MODES OCCUR ONLY AT A LOW FREQUENCY	32
FIGURE 5.9: MODE SHAPES FOR THE FIRST SIX NORMAL MODES OF FREE VIBRATION IN THE CONSTRAINED FEM MODEL	34
FIGURE 5.10: MESH FINENESS STUDY RESULTS	36
FIGURE 5.11: DENSITY AND POISSON'S RATIO KEPT CONSTANT, AND YOUNG'S MODULUS IS VARIED. DENSITY = 8570 KG/M³, POISSON'S RATIO = 0.4	38
FIGURE 5.12: DENSITY AND YOUNG'S MODULUS KEPT CONSTANT, AND POISSON'S RATIO IS VARIED. DENSITY = 8570 KG/M³, YOUNG'S MODULUS = 105 GPA	39
FIGURE 5.13: POISSON'S RATIO AND YOUNG'S MODULUS KEPT CONSTANT, AND DENSITY IS VARIED. POISSON'S RATIO = 0.4, YOUNG'S MODULUS = 105 GPA	40
FIGURE 5.14: EXPERIMENTAL (A) VS SIMULATION (B) RESULTS FOR NB RECTANGULAR PARALLELEPIPED.....	41

FIGURE 5.15: EXPERIMENTAL (A) VS SIMULATION (B) RESULTS FOR A 1 MM THICK, 10 MM DIAMETER NB DISC 42

FIGURE 5.17: EXPERIMENTAL (A) VS SIMULATION (B) RESULTS FOR A HEXAGONAL STEEL NUT 43

FIGURE 5.18: EXPERIMENTAL RESULTS VS SIMULATION RESULTS. RESONANCE FREQUENCIES CORRESPONDING TO MODE NUMBERS 10, 11,16, 19, 20, 22, 24, 26, 28, 29 AND 30 FROM THE SIMULATION RESULTS DO NOT SHOW UP IN THE EXPERIMENTAL FREQUENCY RESPONSE..... 45

FIGURE 5.19: INHOMOGENEOUS MODEL PICTORIAL REPRESENTATION (A) AND ABAQUS MODEL (B) 47

FIGURE 5.20: HOMOGENEOUS VS INHOMOGENEOUS MATERIAL PROPERTY MODEL RESULTS 48

LIST OF TABLES

TABLE 5.1: EXPERIMENTAL FREQUENCY RESPONSE (LOW FREQUENCY RANGE) VS SIMULATION RESULTS-CONSTRAINED VS SIMULATION RESULTS-UNCONSTRAINED.....	33
TABLE 5.3: DIFFERENT MATERIAL PROPERTY VALUES CHOSEN FOR THE PARAMETRIC STUDY	37
TABLE 5.4: MATCHING FREQUENCIES BETWEEN EXPERIMENT AND SIMULATION OF NB RECTANGULAR PARALLELEPIPED	44
TABLE 5.2: MESH FINENESS STUDY COMPARISON.....	58
TABLE 5.5: CONSTRAINED MODEL VS UNCONSTRAINED MODEL – FULL COMPARISON.....	61
TABLE 5.6: PARAMETRIC STUDY DATA	63
TABLE 5.7: HOMOGENEOUS VS INHOMOGENEOUS MODEL RESULTS	67

NOMENCLATURE

C_{ijkl}	Elastic modulus tensor
E	Young's modulus [GPa]
ν	Poisson's ratio
Q	Quality factor
f	Frequency corresponding to peak [Hz]
Δf	Full width of the peak at half power [Hz]
$[M]$	Mass matrix
$[K]$	Stiffness matrix
$\{\ddot{u}\}$	Acceleration vector
$\{u\}$	Displacement vector
ω^2	Eigenvalue
$\{U\}$	Eigenvector
f_e	Eigenfrequency
error% _n	Percentage error of a mode for n elements
f_{\max}	Mode frequency for the highest number of elements [Hz]
f_n	Mode frequency for n elements [Hz]

ABBREVIATIONS

RUS	Resonant Ultrasound Spectroscopy
FEM	Finite Element Method
C3D8	Continuum 3D 8 node

ESS European Spallation Source

ABSTRACT

The objective of this thesis is to validate Resonant Ultrasound Spectroscopy (RUS) as a non-destructive evaluation tool that can be used to study effects of radiation on the mechanical properties of a material, mainly its elastic constants. RUS involves experimentally measuring the resonant frequencies of a sample and calculating the elastic constants based on these measurements. Finite Element Method (FEM) is used to get the frequencies of the modes of free vibration for the sample model. This result depends on the elastic constant values used in the FEM simulation. Studies were conducted to confirm the accuracy of the FEM model, and determine the right configuration and parameters to use for the simulation. Assuming uniform and isotropic elastic property changes, the effects of radiation damage can be quantified by obtaining a set of matching resonant frequencies between the experimental and FEM simulation results, before and after irradiating the sample. This is done by adjusting the elastic constant values used in the simulation so that the results match with the experimentally obtained resonant frequencies. With powerful enough equipment, even real time monitoring is possible in harsh environments, thus pointing out imminent failure.

CHAPTER 1 – INTRODUCTION

1.1 Introduction

Charged particles in an accelerator gain kinetic energy and thus momentum as the accelerator magnets propel them through a vacuum tube. When they gain enough energy, they tend to collide with each other and move erratically away from the direction of propulsion. Since these subatomic particles are not bound by a physical boundary, they pass through the tube wall and come in contact with the accelerator components outside the tube. This acts as a fast particle irradiation, the particles being protons, electrons etc. Figure 1.1 shows a crude representation of how this might look.

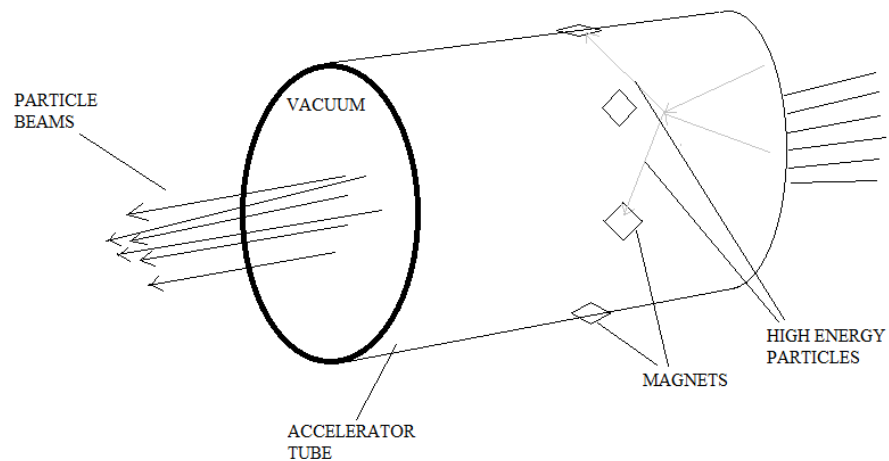


Figure 1.1: Particle irradiation in accelerators

The European Spallation Source (ESS) is interested in using non-destructive evaluation for testing accelerator components, mainly the niobium electromagnets their proton accelerator uses.

Non-destructive testing methods have become more dominant in the engineering industry in recent times, mostly due to their reliability and repeatability. Since the sample is intact in the testing process, real time testing is a possibility in most cases. This allows for accurate failure prediction, which gives these testing methods a step up above theoretical prediction of failure and prediction through post-failure analysis.

Measuring the elastic constants of a material through non-destructive testing methods in harsh environments, mostly neutron and proton irradiation, is the main purpose of this research. Specifically, it involves using resonant ultrasound spectroscopy to evaluate the elastic constants of a material in real time to observe any changes.

Resonant ultrasound spectroscopy, or RUS, is a technique in which one measures the natural frequencies of elastic vibration for several normal modes of a sample, then processes these along with the shape and mass of the sample in a computer [1]. This basically means that the natural frequencies are measured for a sample and then the elastic constants are obtained from the measured frequencies by applying a non-linear inversion algorithm. Traditionally the inversion process, referred to as the inverse problem, involved the Rayleigh Ritz method [2]. With recent technological advances in computation power, this has been replaced with the Finite Element Method, or FEM for short. In FEM, the inverse method involves creating a finite element model of the sample with an initial guess of the material properties and matching the resulting natural frequencies calculated by the FEM software with the measured frequencies. If the results do not match, the material properties are changed and the process is repeated until the error between the measured and calculated natural frequency spectrum is within acceptable limits.

Currently the information we have about radiation damage to materials mostly covers micro-scale changes such as dislocations and void formations in the structure. But studying the effect of varying elastic constants, mainly the Young's modulus, on the natural frequency through FEM simulations and comparing it to measured natural frequencies through RUS after irradiation would help us understand if the material behaves as if it has undergone changes to its bulk properties isotropically. It is also worth observing the factors influencing the natural frequencies of a material experimentally, as opposed to just theoretical models done so far.

The main material chosen for testing here is Niobium (Nb) for its isotropic nature and its application as a superconducting accelerator [3], thus exposing it to a fair amount of proton irradiation. The main subjects of interest covered in this thesis include the repeatability of experimentally measured natural frequencies of different geometries of niobium, validity of FEM simulations with isotropic property change assumptions, and the process for matching frequency results from the experiment to the simulation, before and after irradiation through trial and error manipulation of material properties in the simulation.

CHAPTER 2 – LITERATURE REVIEW

2.1 Effects of radiation

Materials when exposed to intense radiation undergo various changes. Let's take metal parts in a nuclear reactor environment for example. These changes are considered negative from the perspective of the parts' intended function. Radiation damage is one of the main negative effects of radiation exposure which is basically nuclear radiation causing a disruption in the material's crystal lattice by displacing its atoms [4]. This affects the material's mechanical behavior in the following ways:

1. Hardening
2. Embrittlement and fracture
3. Swelling
4. Irradiation creep

Hardening occurs due to exposure to fast neutrons and high temperature within the reactor environment, which results in an increase in yield stress and ultimate tensile stress of the material. Neutron bombardment also causes a change in the material's elastic constants which were predicted by Dienes through theoretical studies [5]. Wang, Ngai, and Wang observed experimentally that the Poisson's ratio decreases with decrease in ductility of metallic glasses during annealing [6]. However, there is a certain depth of penetration associated with proton irradiation [7] as shown in figure 2.1. This would likely cause surface hardening and embrittlement rather than reduce the bulk ductility of the material, thus not affecting the Poisson's ratio by a large amount depending on the geometry. The presence of peak damage is because of point defect concentration i.e.,

supersaturation of vacancies and interstitial atoms which is characteristic of radiation damage.

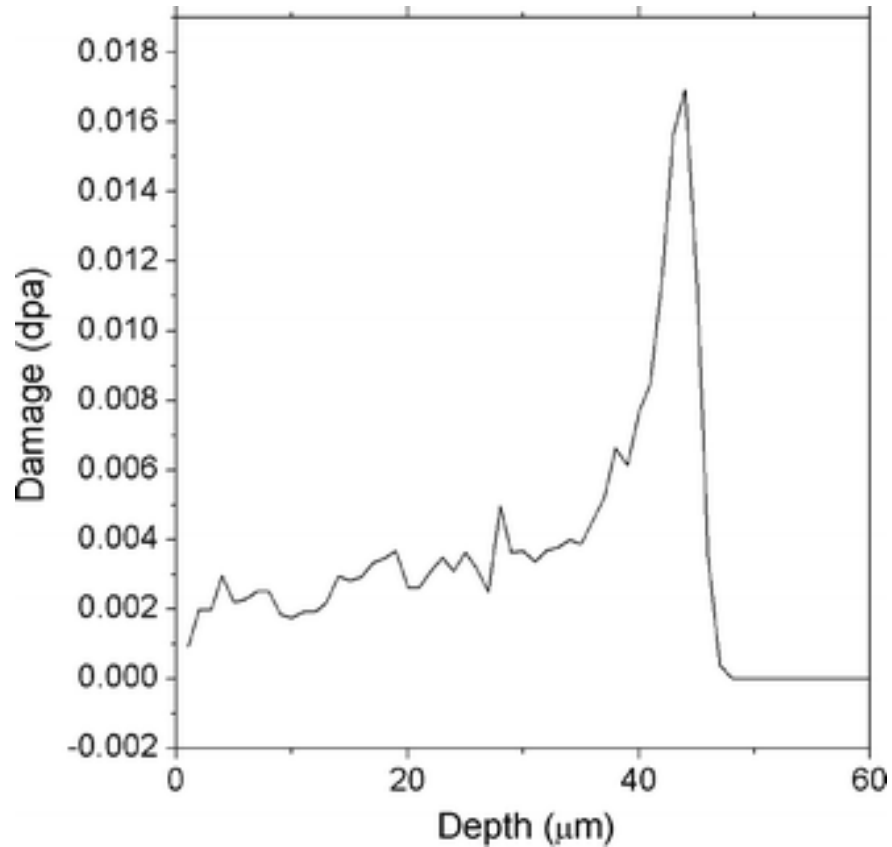


Figure 2.1: n_{dpa} for 2.6 MeV protons at fluence of 1017 p/cm^2 for Zirconium, calculated using SRIM 2003 code [7]

Materials when subjected to intense neutron radiation end up accumulating dislocations and voids causing an increase in their volume and a resulting decrease in their density. This is known as Neutron induced swelling. Irradiation causes a disruption in the atomic structure, where an atom is displaced from its site causing a vacancy. The displaced atom comes to rest in a different location in the lattice structure of the material as an interstitial atom [8]. This interstitial atom causes an imbalance in the electron-

proton charge. This type of damage is caused by high energy neutrons as well as proton and electron particles. Figure 2.2 shows a schematic representation of this effect.

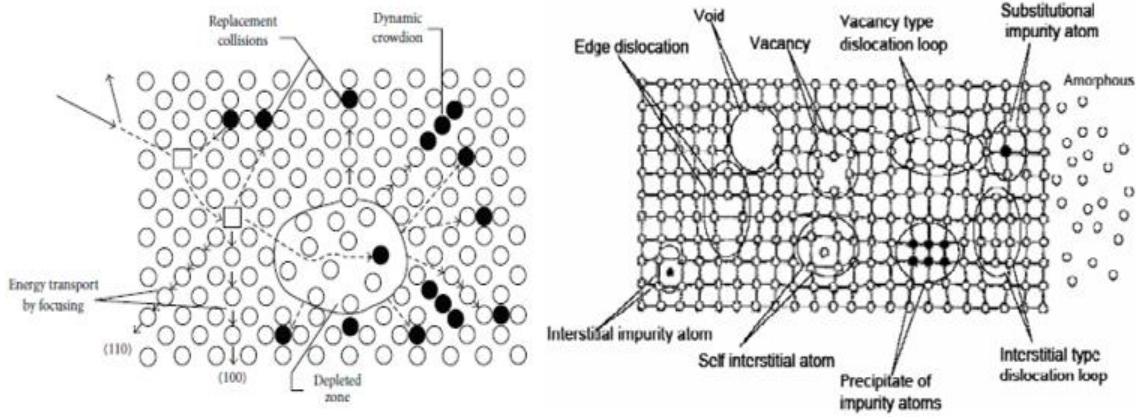


Figure 2.2: Neutron damage [8], [9].

It was observed that in a fast reactor environment, pure nickel undergoes up to 7 % change in density [10] as seen in figure 2.3. The dependence on temperature is due to thermal expansion contributing to the swelling effect up to a point after which ductile to brittle transition due to temperature effects becomes more apparent, especially when it is body centered cubic iron.

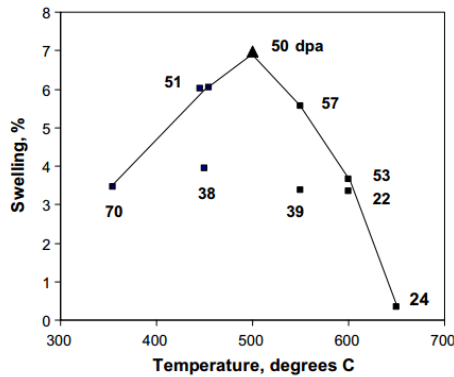


Figure 2.3: Swelling% ($\Delta\rho/\rho$) observed in pure nickel irradiated in BOR-60 reactor (squares) and BN-350 (triangle at 500°C only) vs. irradiation temperature. Dpa (displacements per atom) levels are indicated for each data point [10]

The effect of electron irradiation on the Young's Modulus of copper was studied experimentally by Dieckamp and Sosin [11]. Figure 2.4 shows their results. The flux mentioned here refers to integrated flux (over time) which is basically fluence, which has the units of electrons/cm².

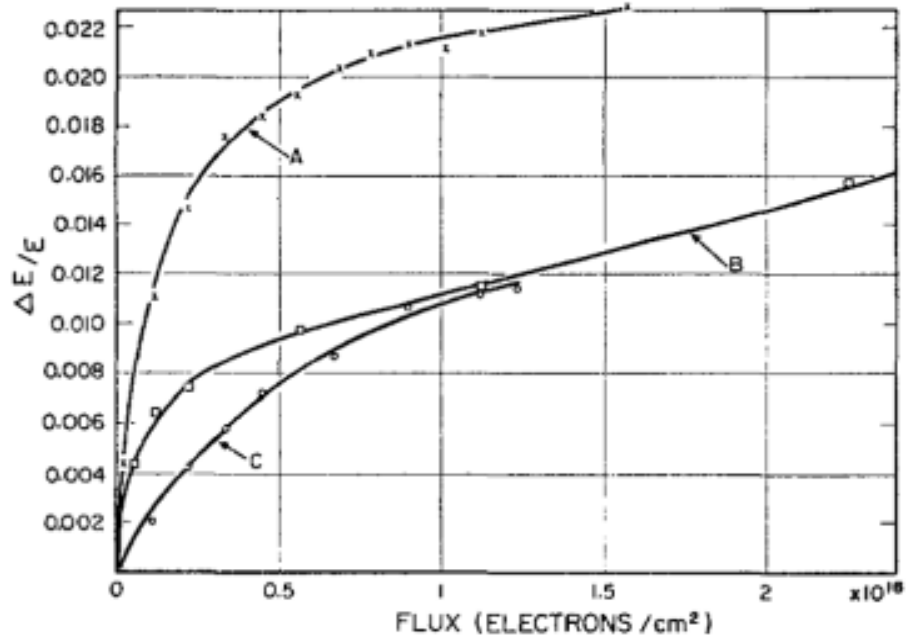


Figure 2.4: Fractional change in Young's modulus of 99.99 % copper as a function of exposure to 1-MeV electrons [11]. The three different lines are for three different specimens based on heat treatment: A was slightly cold worked, B was annealed and C was heavily cold worked.

A study conducted on the effect of vacancies on the Young's modulus of Zirconium showed that the anisotropy of Young's modulus decreased with increase in the concentration of vacancies [12]. A study of the effect of 2.6 MeV proton irradiation on Zircaloy-4 and pre-hydrated Zircaloy shows a decrease in nano-hardness and Young's modulus [7] as shown in figure 2.5.

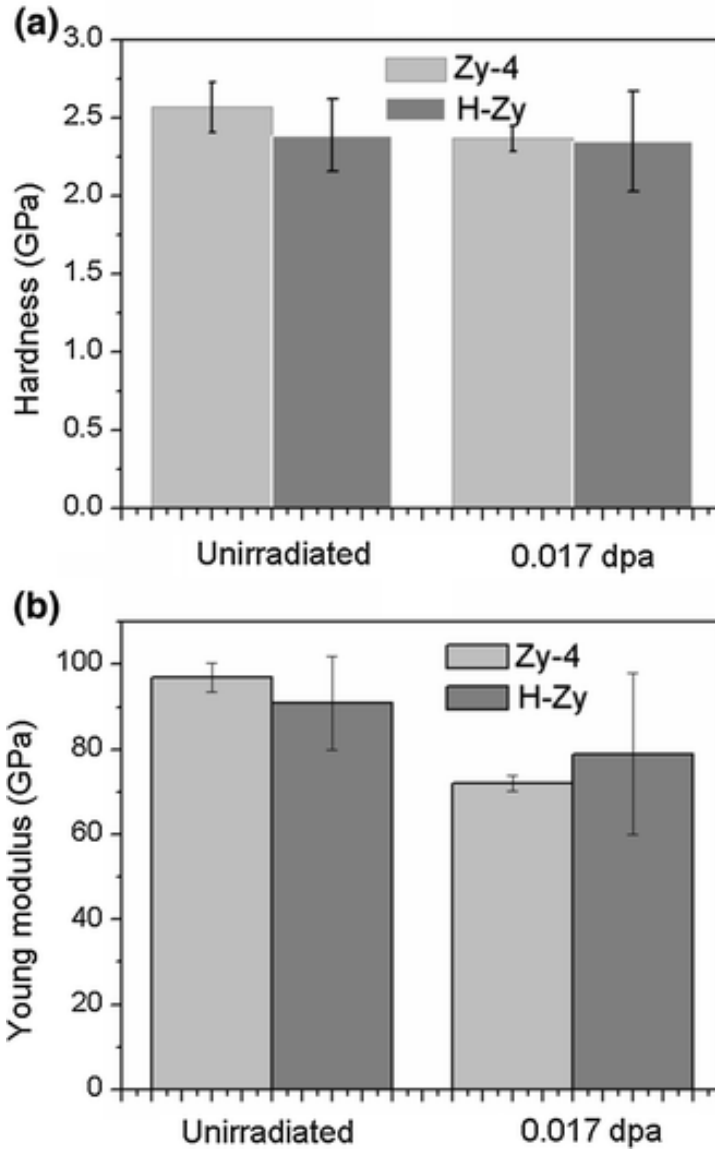


Figure 2.5: Nano-hardness (a) and Young's modulus (b) of Zy-4 and H-Zy samples before and after 2.6 MeV proton irradiation [7]

We can observe that the change in Young's modulus depends on the type of irradiation and varies from material to material. We also see that the main changes that occur during proton and neutron irradiation are to the density and the Young's modulus. One of the non-destructive evaluation practices for evaluating elastic constants, mainly Young's modulus, is Resonant Ultrasound Spectroscopy.

2.2 Resonant Ultrasound Spectroscopy

RUS focuses on digital data analysis more than on experimental technique. In said data analysis, there is the forward problem which involves calculating the natural frequencies in terms of elastic constants and sample geometry and mass. The second part of the data analysis is the inverse problem which involves applying a non-linear inversion algorithm to find the elastic constants from the measured natural frequencies. The inverse problem, traditionally, involved the Rayleigh Ritz method [2] but it has been proven that the Finite Element Method (FEM) is just as good an approach as the Rayleigh Ritz method [13]. Due to recent technological advances in computational power, RUS has seen a significant growth in its popularity since a major drawback was that the FEM inverse problem would take too long.

For an isotropic cube or nearly cubic parallelepiped, the frequencies of the free vibration modes depend heavily on the elastic modulus tensor C_{ijkl} [14] due to the material stiffness matrix being dependent on it. The elastic tensor for isotropic materials reduces to the form shown in equation 2.1 [15] where the matrix consists of three non-zero components and is symmetrical along the diagonal. This significantly reduces computation time given the large number of elements this matrix is assigned to.

$$C_{ijkl} = \frac{E}{(1+\nu)(1-2\nu)} \begin{bmatrix} 1-\nu & \nu & \nu & 0 & 0 & 0 \\ \nu & 1-\nu & \nu & 0 & 0 & 0 \\ \nu & \nu & 1-\nu & 0 & 0 & 0 \\ 0 & 0 & 0 & \frac{(1-2\nu)}{2} & 0 & 0 \\ 0 & 0 & 0 & 0 & \frac{(1-2\nu)}{2} & 0 \\ 0 & 0 & 0 & 0 & 0 & \frac{(1-2\nu)}{2} \end{bmatrix} \quad (2.1)$$

Here, E is the Young's modulus and ν is the Poisson's ratio. This makes it simple for estimating the elastic constants for an isotropic material, namely the Young's modulus and Poisson's ratio, through the FEM inverse problem by trial and error adjustment.

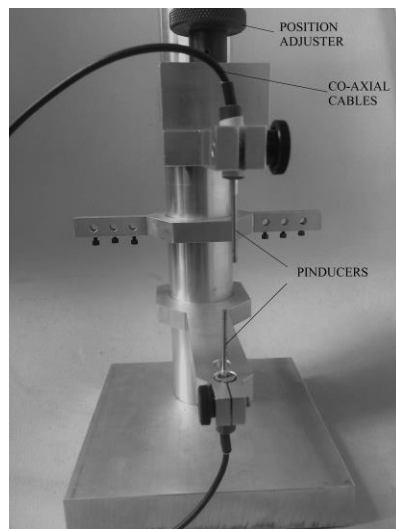
RUS has been proven to be particularly accurate in studies of quasicrystals, given their elastic isotropy unlike conventional crystals [16]. Since the linear elasticity is isotropic, the velocity of sound is remains same in all directions.

Even though niobium is thought to have a body centered cubic structure up to its melting point, it has been observed that it displays anisotropic thermal expansion, martensitic in character, that is not consistent with cubic crystal structures at low temperatures [17]

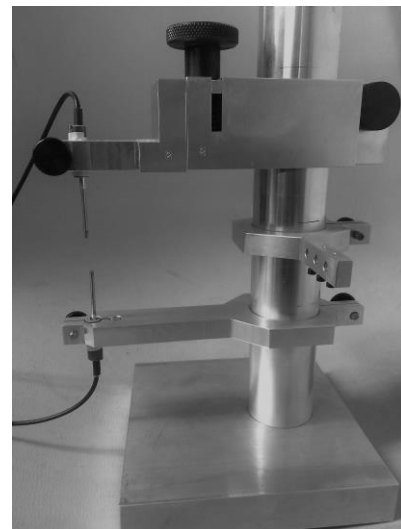
CHAPTER 3 – RUS: EXPERIMENTAL SETUP

3.1 Setup

The simplicity in the experimental setup of RUS makes it extremely viable in the current material testing field. The equipment involved includes several piezoelectric transducers, commonly referred to as pinducers given their shape. One pinducer acts as the source of excitation and the others would receive the response signal, both the signals being processed by a network analyzer. The process is controlled via a PC user interface. Given the sample geometry and the testing environment, the setup for holding the pinducers and the sample could get slightly complicated but for most cases two or three pinducers with different holders would suffice. If the sample is small enough such that its center of mass will not make it tip over when held between the pinducers with point contact, the two-pin setup, as shown in figure 3.1, can be used.



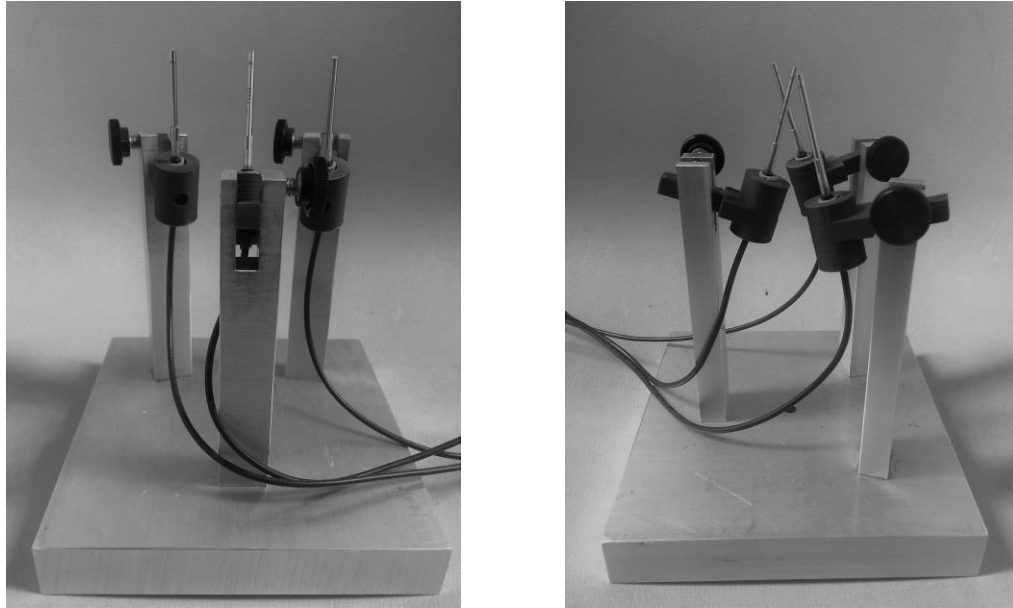
(a) Front view



(b) Side View

Figure 3.1: RUS two-pin setup for small samples

If the size and mass of the sample is too big or if the sample geometry does not allow for a two-pin setup, a three-pin setup, as shown in figure 3.2, is preferred



(a) Front view

(b) Side view

Figure 3.2: RUS three-pin setup for larger samples

In this research, a small niobium rectangular parallelepiped (dimensions 5.03 mm x 5.03 mm x 3.2 mm) is used for the most part. To establish repeatability for multiple geometries and materials, two niobium discs (10 mm diameter, 3.2 mm and 1 mm thick respectively), an aluminum rectangular parallelepiped (6 mm x 6 mm x 8 mm) and a M6 hexagonal steel nut were also tested. Given these geometries, the two-pin setup is used.

The pinducers used are the standard type model VP-1093, manufactured by Valpey Fisher corporation. They have a crystal diameter of 1.5 mm and a frequency range of 1 kHz to 10 MHz.

To both generate the frequencies and to read the responses, Zurich Instrument's HF2LI lock-in amplifier is used. A LabVIEW program based software dubbed ziControl

enables us to interface the pinducers with the lock-in amplifier. The reason a lock-in amplifier is used is because of its ability to single out the required component of the signal at a specific frequency and phase, while rejecting noise signals at frequencies other than the reference frequency [4].

3.2 Procedure

The schematic representation of the data acquisition for the RUS experiment is shown in figure 3.3.

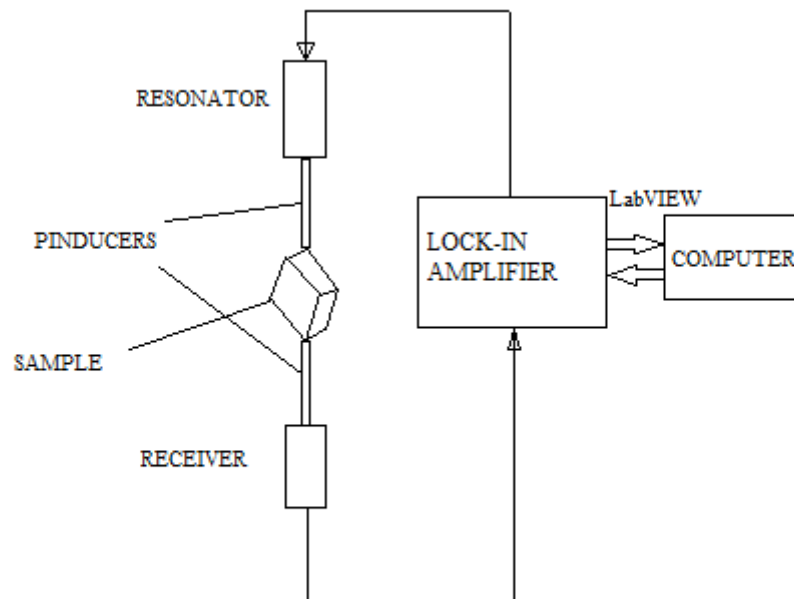


Figure 3.3: RUS experiment data acquisition

For accurate results, there should be minimal loading on the pinducers due to the sample. This means that the sample should stand on its own on top of the bottom pinducer while the top of the sample is held in place by point contact with the top pinducer. Each pinducer in the two-pin setup are held at one end, which means that the

other end behaves similar to the free end of a cantilever beam. This way, once the appropriate distance between the two pinducers is set with the position adjuster, the sample can be gently squeezed into position such that there is light point contact between the pinducer ends and the opposite corners of the sample. This ensures minimum contact pressure between the pinducers and the sample. This contact pressure can shift the measured natural frequency up to more than 1 kHz [18].

The lock-in amplifier has a resonator and a sweep function, which means that it can generate a range of frequencies which is perfect for RUS. This sweep function is used to generate a range of frequencies of interest, which is usually 1 kHz to 500 kHz for the Niobium sample used. The amplitude output chosen in the Zurich instruments interface, 'ziControl', acts as an amplifier of sorts which means the peaks are clearer, the higher the output amplitude. The response is received by the lock-in amplifier which filters out the noise and keeps the actual response which is in the reference frequency range. This is displayed as the amplitude vs frequency response graph in the ziControl GUI on the computer. Figure 3.4 shows an example of such a response for the Niobium parallelepiped with 2000 data points. The distinguished peaks can be clearly observed which represent the natural frequency of a sample with given geometry and material properties.

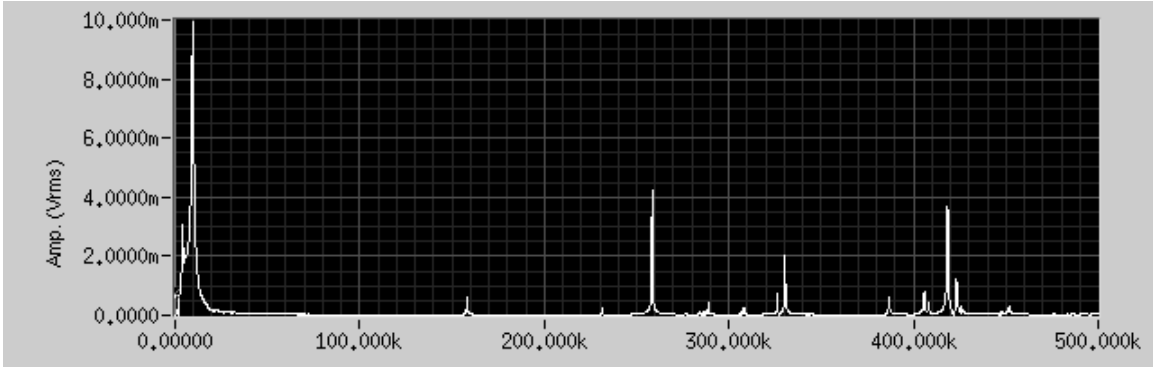


Figure 3.4: Amplitude (Vrms in V, m representing $\times 10^{-3}$) vs Frequency (Hz). Here the range considered is from 0 Hz to 500 kHz. The peaks represent the natural frequencies of the sample.

Not only is a graph of the frequency response obtained from this process, we also get a data file in *.csv format containing the amplitude corresponding to each frequency data point. This data file is crucial for the data processing process, since a low-resolution image of a graph cannot be used to accurately pinpoint the natural frequencies. From this data file, the natural frequencies can be extracted and so can the quality factor of the corresponding peaks, using a free Matlab code, which is discussed in the section that follows. Here, quality factor, is defined as a dimensionless parameter that provides information about the dissipation of elastic energy for each resonance. Mathematically, quality factor, also known as Q factor, is given by the natural frequency divided by the full width of the corresponding peak at half-power (equation 3.2.1).

$$Q = \frac{f}{\Delta f} \quad (3.1)$$

f is the frequency corresponding to a peak in the response and Δf is the width of the peak at half power. We also get a phase vs frequency response from the experiment as shown in figure 3.5. The sensitivity of this phase information helps us identify the peaks

correctly when the value of Q factor is low or if more than one mode is present in a small frequency window.

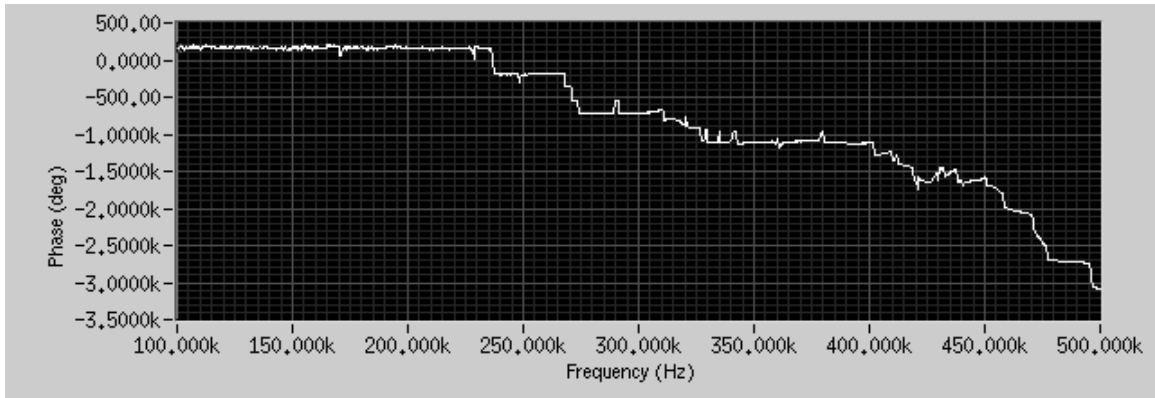


Figure 3.5: Phase(degrees) vs Frequency(Hz) for an Al parallelepiped (dimensions 5 mm x 5 mm x 8 mm) in the frequency range 100 kHz to 500 kHz

3.3 Data processing

Once we get the *.csv file we use a free Matlab code from Leighton and Watson, which can be accessed at reference [19], to extract the natural frequencies and the corresponding Q factors. The *.csv file is opened in Microsoft Excel and converted to *.dat format. This is loaded into the Matlab code named Fitspectra which gives us a GUI as shown in figure 3.6.

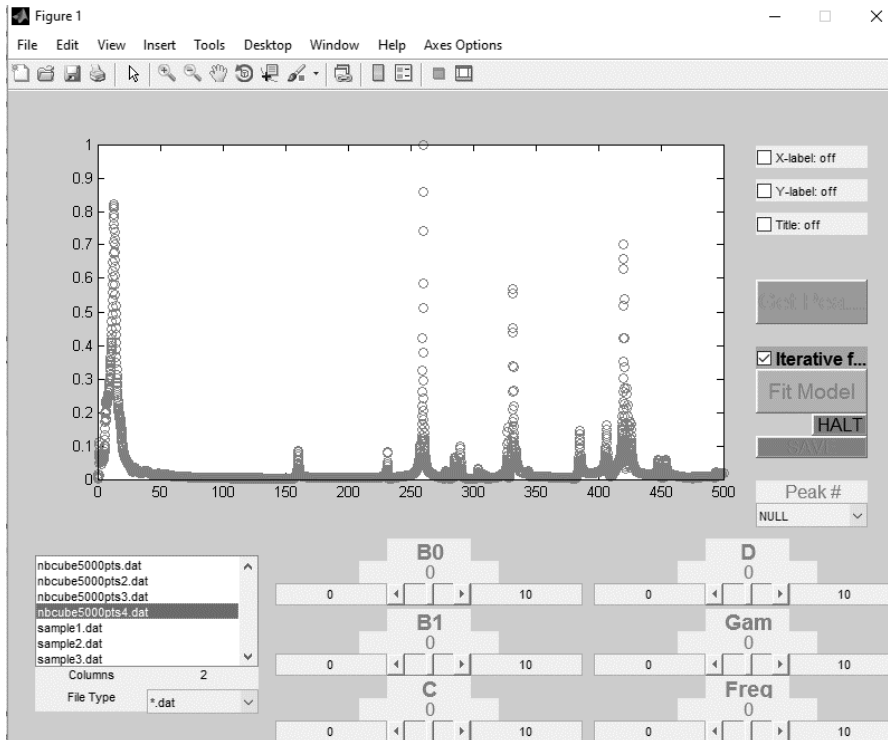


Figure 3.6: Fitspectra GUI in Matlab with a data file from the results of Niobium parallelepiped loaded in.

Each peak is selected individually and the curve is fit using the fit model function in the code which provides us with an approximate fit. The sliders in the GUI allows for adjusting the curve fit to accurately match the visible data points. Figure 3.7 shows how the Q factor is calculated for a frequency response, given the curve fit is based on data points imported from the data file. Figure 3.8 shows the curve fit after adjusting the sliders. Then the save button is pressed on the GUI to save the frequency and Q factor to a separate file.

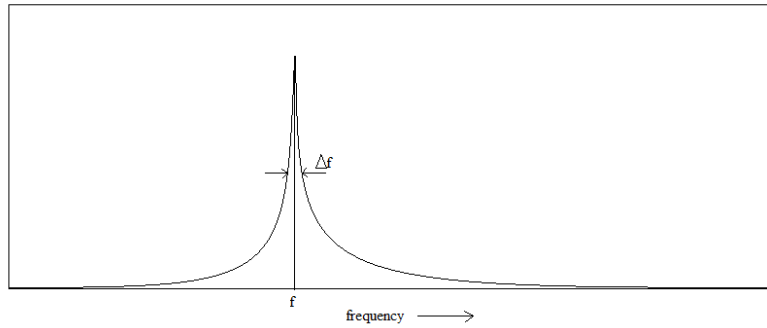


Figure 3.7: Q factor measurement. $Q = f/\Delta f$

This process is repeated for each visible peak to get all the natural frequencies and the corresponding Q factors in the chosen frequency range. This natural frequency information will be used to compare with the simulation results.

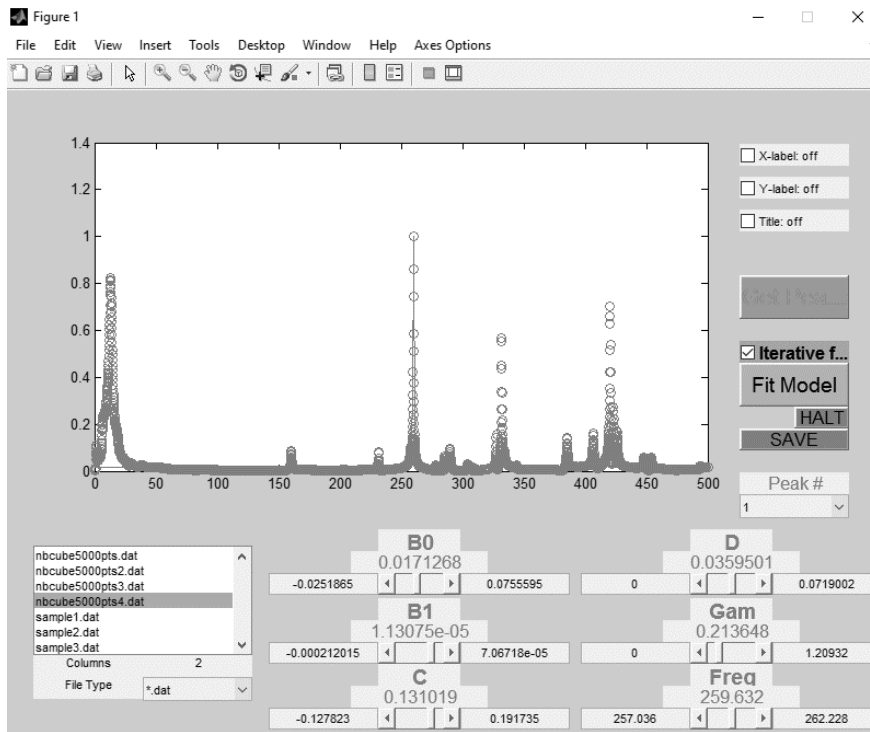


Figure 3.8: Adjusted curve fit which saves the frequency and Q factor information of the peaks.

CHAPTER 4 – FINITE ELEMENT METHOD: ABAQUS SIMULATION

4.1 Simulation procedure

FEM has been proven to be a good approach when tackling the inverse problem part of the RUS process. It involves making an initial guess of Young's Modulus and Poisson's ratio for the FEM model, obtaining the free vibration modal analysis results from FEM, and comparing the resonance frequencies with the experiment. If the error exceeds allowed limits, the Young's Modulus is adjusted and the FEM results are obtained again. This process is carried out until the error is low enough. The model is created on the commercial finite element software ABAQUS. Figure 4.1 shows the flowchart describing this process.

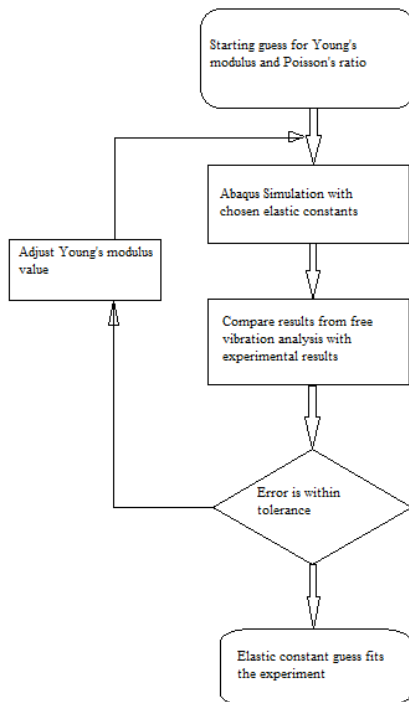


Figure 4.1: Flowchart explaining the inverse problem of RUS

The dynamic equation for undamped free vibration is given by equation 4.1.1.

$$[M]\{\ddot{u}\} + [K]\{u\} = \{0\} \quad (4.1)$$

[M] is the mass matrix, $\{\ddot{u}\}$ is the acceleration vector, [K] is the stiffness matrix and $\{u\}$ is the displacement vector. The right-hand side of the equation is considered zero since we are interested in the free vibration response. The damping effect is less than 10 % which is negligible and can be ignored. This is the basic equation to be solved for each element of the model. The mass matrix is dependent on the density and shape factor matrix (derived from the Jacobian), and the stiffness matrix is dependent on the elastic tensor matrix (given by equation 2.1 for isotropic materials) and the shape factor matrix. The solution to this equation is of the form

$$\{u\}(t) = \{U\}e^{i\omega t}, \quad \{\ddot{u}\}(t) = -\omega^2\{U\}e^{i\omega t} \quad (4.2)$$

Plugging this into equation 4.1, we get

$$([K] - \omega^2[M])\{U\}e^{i\omega t} = \{0\} \quad (4.3)$$

The non-trivial solution to this would be the eigenvalue problem given by

$$\det ([K] - \omega^2[M]) = 0 \quad (4.4)$$

$$\omega = 2\pi f_e \quad (4.5)$$

ω^2 is the eigenvalue, f_e the eigenfrequency and $\{U\}$ the eigenvector.

A 3-D model part is created with the same dimensions as the sample. The material properties are then input, then the section is created pertaining to those properties and applied to the part. The instance is made independent of mesh under assembly options.

The step is then created with the linear perturbation module along with frequency analysis. The model is then meshed with appropriate element type and count. The job input file is written and the job is submitted. The built-in Lanczos solver [20] calculates the eigenvalues and thus eigenfrequencies. The Lanczos method merely involves normalization of computed eigenvectors to a unit value of generalized mass. After running, we observe the results which shows the mode shapes for each normal mode of vibration. To get a report file with the mode numbers and the corresponding frequencies, the history output feature is used to create XY-data which can be reported to a *.rpt file. This file can be edited with the open source software, Notepad++.

4.1.1 Parameters/Variables

There are various parameters and settings which influence the results of the simulation. It is observed that the value of the natural frequencies extracted by the simulation shifts with change in the density, Young's modulus and the Poisson's ratio values used for material property definition. It also shifts a little bit based on the mesh fineness, thus giving rise to a need for optimum element count that gives minimum error while simultaneously minimizing computation time. One important factor that is overlooked in simulations of this type with small sized samples is the element type. The element shape factor matrix influences both the mass and stiffness matrices which in turn influence the solution of the eigenvalue problem. The shape of the element used for cubic or parallelepiped geometries should be regular hexahedral 8 node elements, or brick elements. For a disc shaped geometry, 4 node tetrahedral elements give the most accurate results. There is also the issue of reduced integration elements giving erroneous results. Complicated finite element problems use numerical integration methods, mainly the

Gaussian quadrature method, to calculate the element stiffness matrix. For the function to be integrated, a number of points are calculated and their positions are optimized, known as Gaussian co-ordinates. For each of these points, the function is multiplied by an optimized weight function. Then these are added together to calculate the integral. Reduced integration uses a lesser number of Gaussian co-ordinates when solving the integral. Using reduced integration will basically mean it will take less time to run the analysis but it could have a significant effect on the accuracy of the element for a given problem. This is mainly observed in the form of the hourglassing effect, where the integration point on the element appears to be under zero stress thus causing a bending mode of deformation counting as a zero-energy mode. This manifests itself as mode shapes where the overall geometry is retained but individual elements appear to be severely deformed into a patchwork of zig-zag or hourglass-like shapes. The error in the results increases with the coarseness of the mesh [21].

4.1.2 Parametric study

A study had to be conducted to see how the natural frequencies obtained from the simulation behave with varying parameters. This was done by using a simple python script included in appendix A. Basically the script varies the *.inp file created for a job in ABAQUS for separate trials to have different combinations of material properties, thus creating as many input files as there are said material property combinations. The script is run in the ABAQUS command prompt which gives us separate output files for each combination in *.odb format which can be opened in the ABAQUS GUI to observe mode shapes and get the required report files.

CHAPTER 5 – RESULTS AND ANALYSIS

5.1 Repeatability of the experiment

As with any experimental method, RUS comes with its own set of uncertainties throughout the whole process. Figure 5.1 shows the RUS forward modeling and model inversion process, which gives us an idea of the various sources of error possible.

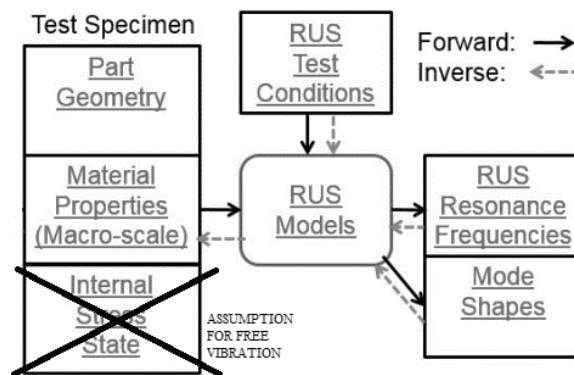
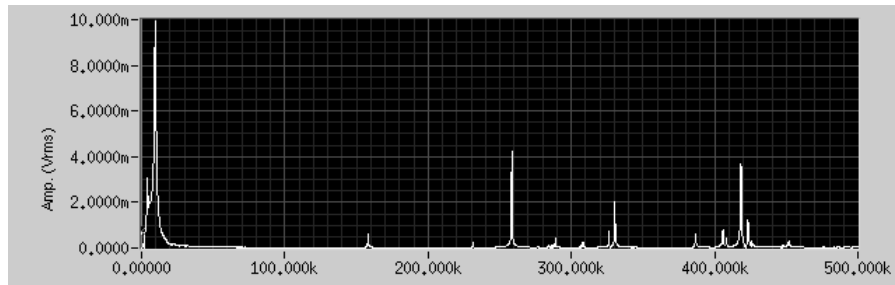


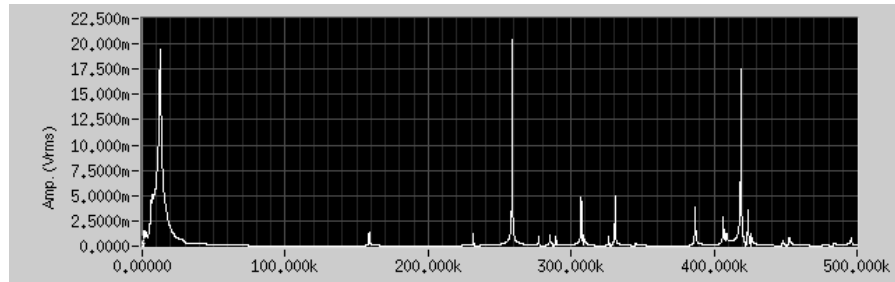
Figure 5.1: Representation of the forward model and the inverse problem in RUS [22].

One of the main sources of error comes from the RUS testing process itself. On a four-point fixture, for a ½” diameter by 3” long cylindrical Mar-M247 coupon, the standard deviation of thirty measurements was found to be 0.0048 % for static measurements and 0.023 % for measurements where the sample was re-mounted each time [22]. For a two-pin setup similar to the setup used in this research, the variability was 1.5 times that of the four-pin setup, i.e., a standard deviation of 0.0072 % for thirty static measurements and 0.0345 % when the sample was re-mounted between measurements. Even though the absolute deviation is still low, it is worth establishing decent repeatability, even with re-mounting the sample.

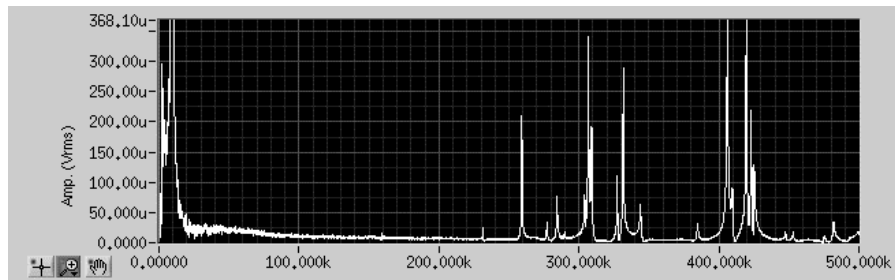
Figure 5.2 shows the frequency response results in 0Hz to 500 kHz range of a 5.03mm x 5.03mm x 3.2mm Niobium rectangular parallelepiped for three separate trials, where the sample was remounted for each trial. The same was done with a Niobium disc with 10mm diameter and 1mm thickness (Figure 5.3), and another disc with the same diameter but 3.2mm thick (Figure 5.4)



(a) Trial 1



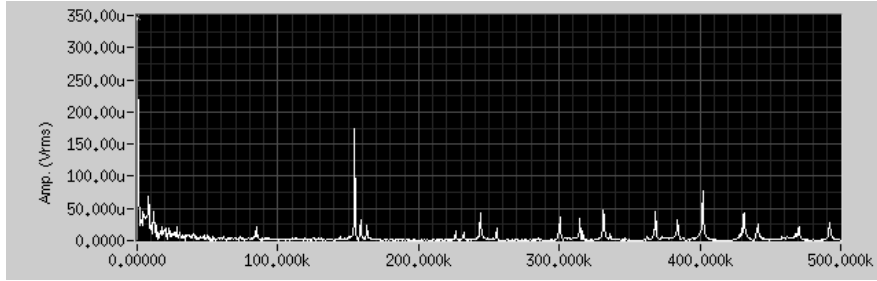
(b) Trial 2



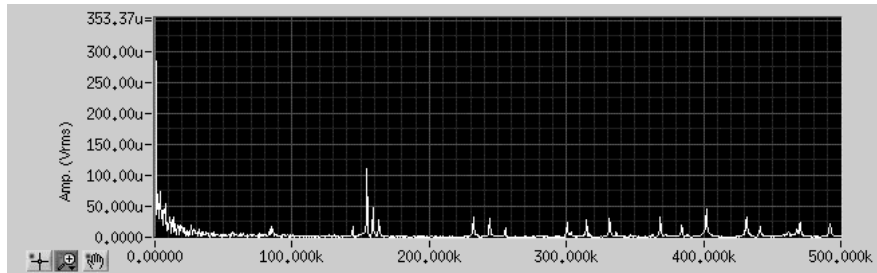
(c) Trial 3

Figure 5.2: Frequency response of Niobium rectangular parallelepiped (0Hz – 500kHz) with 2000 data points on x-axis.

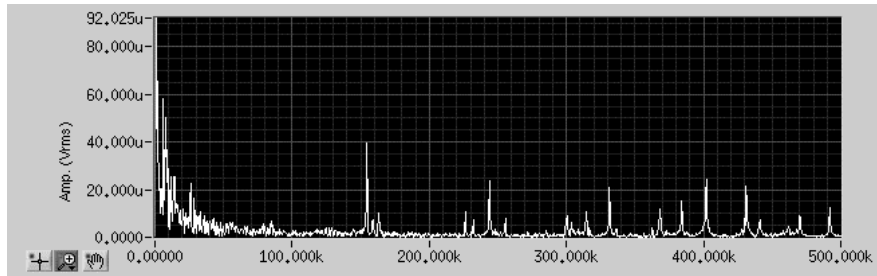
For (a) and (b) the output amplitude chosen was 10V whereas for (c) it was 1V



(a) Trial 1

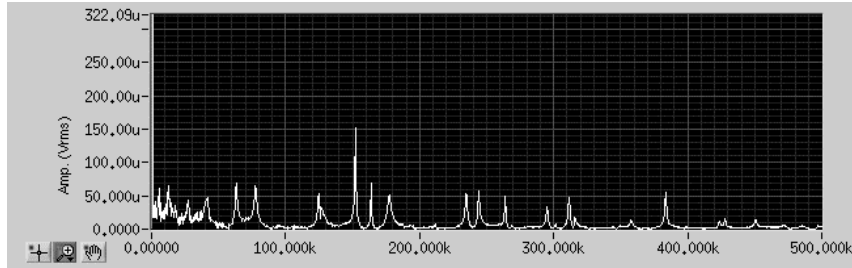


(b) Trial 2

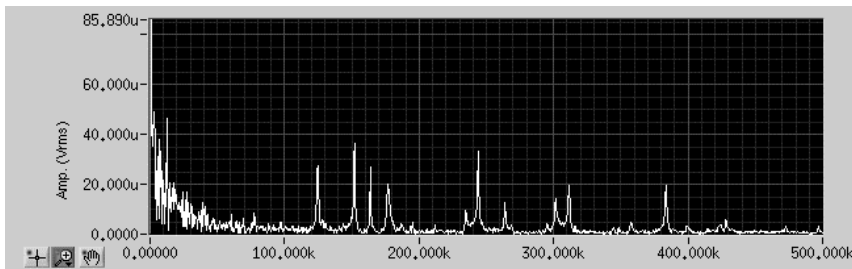


(c) Trial 3

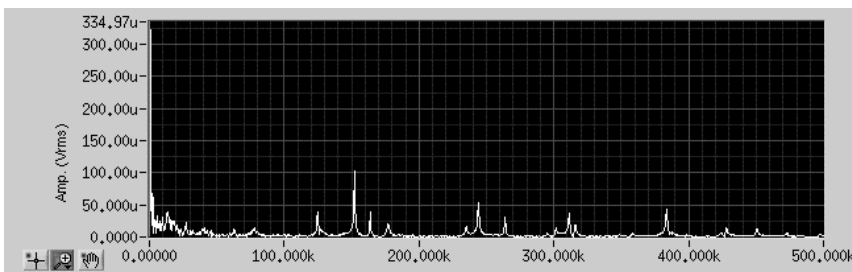
Figure 5.3: Frequency response of Niobium thick disc (10mm diameter, 3.2mm thickness) in frequency range of 0Hz-500kHz with 2000 data points on the x-axis. Output amplitude chosen is 0.1V for all three trials.



(a) Trial 1



(b) Trial 2



(c) Trial 3

Figure 5.4: Frequency response of Niobium thin disc (10mm diameter, 1mm thickness) in frequency range of 0Hz-500kHz with 2000 data points on the x-axis. Output amplitude chosen is 0.1V for all three trials.

We observe in each trial that the frequency results remain the same for a sample for most, if not all, normal modes of vibration. The discrepancy in the amplitude of the peaks can be explained by the fact that in some of the trials the samples might have been held under varying pressure between the pinducers. The orientation of the sample also played a big part even though the Niobium samples are assumed to be isotropic and homogenous, thus attributing errors arising from orientation to imperfections in the

material structure. Any errors in frequency itself could be due to a relatively higher uncertainty for certain mode shapes over others [22]. We can observe that there is not much variation in the resonant frequencies for the rectangular parallelepiped, given that we choose a higher output amplitude, thus being able to minimize the noise in the results. For the discs however, there is slight difficulty in distinguishing actual peaks from noise.

The amplitude variation for each resonant frequency for the rectangular parallelepiped (at same output amplitude chosen) can be explained by the fact that the assumption of perfect homogeneity and absence of defects was made. Thus, the orientation could have played an important role in the results. This is not so apparent in the discs since the orientation for each trial was the exact same, ensured by markings on the sample. The Q factor depends on the amplitude and the variation in the Q factor at individual resonant frequencies could be explained similarly.

5.2 ABAQUS simulation results: Mesh study and constraints

To confirm the validity of mesh settings for the simulations, which is an extremely important parameter that decides the accuracy of the results, a mesh study was conducted where different mesh types and mesh counts were used for the simulations and the results were analyzed. The parallelepiped model constructed in ABAQUS is shown in figure 5.5.

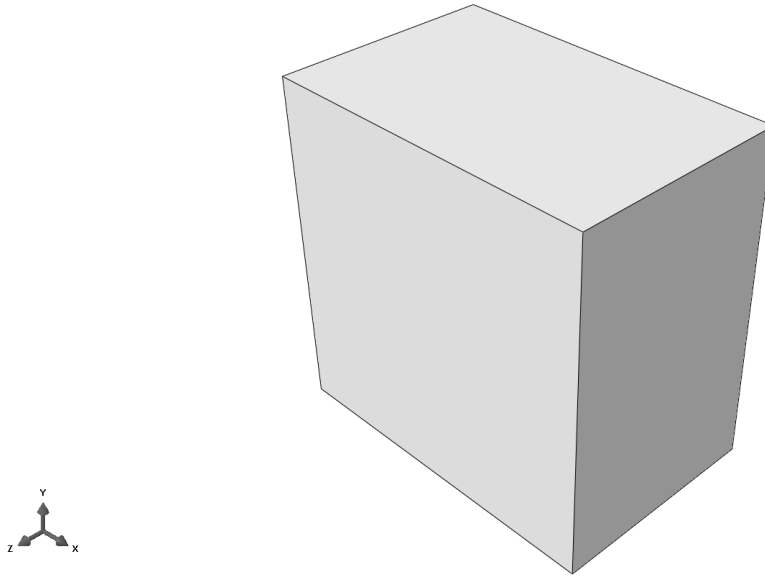


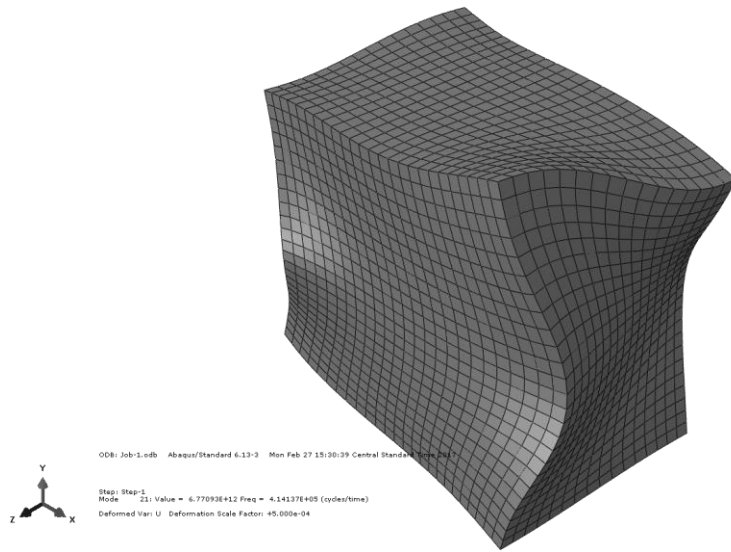
Figure 5.5: Part geometry constructed in the ABAQUS GUI

5.2.1 Mesh type

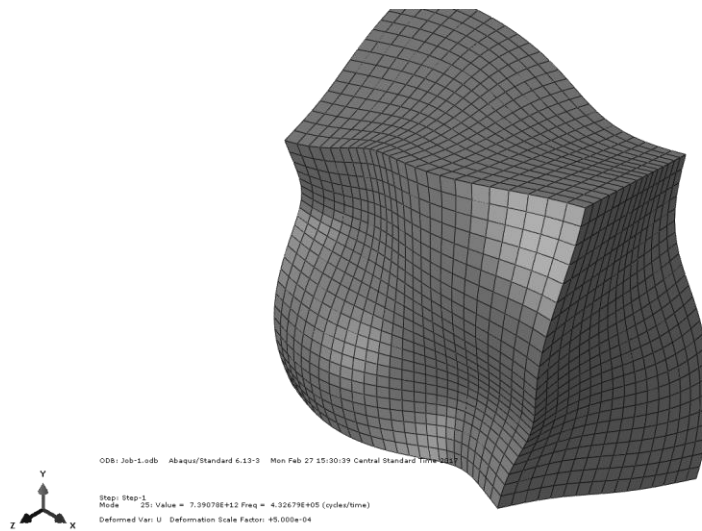
When the wrong type of element is used in a simulation it causes a significant error or even potentially completely invalidates the results, especially when it comes to frequency analysis as we can observe in the following section.

An ABAQUS model was constructed, the rectangular parallelepiped part dimensions being 5.03mm x 5.03mm x 3.2mm. The material properties used were of Niobium [23], with density being 8570 kg/m³, Young's modulus of 105 GPa and a Poisson's ratio of 0.4. A continuum 3-D 8 node element type was first considered without the reduced integration option. This element is referred to by ABAQUS as the C3D8 type. After getting results for this configuration, the element type was changed to the reduced integration type 8 node brick element, i.e. C3D8R type, and another set of natural frequency results were obtained. These two results were compared and the

different mode shapes for two of the mode numbers in each case are shown in figure 5.6 and figure 5.7.

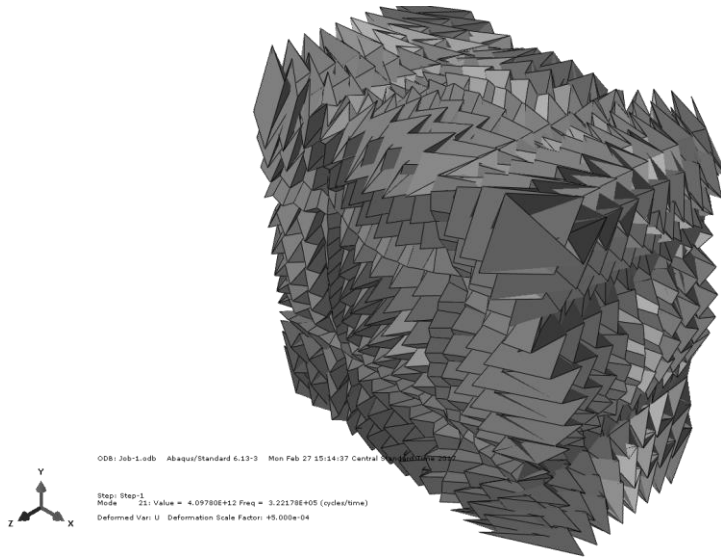


(a) Mode no. 21 – Frequency = 414.137 kHz

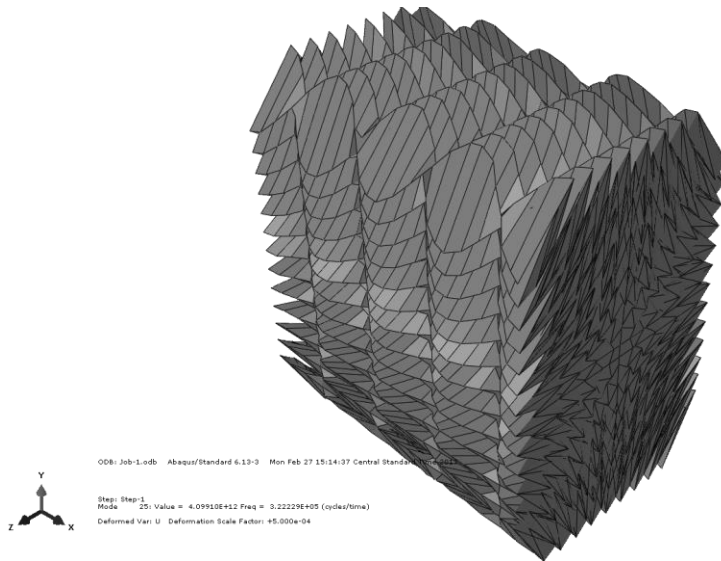


(b) Mode no. 25 – Frequency = 432.679 kHz

Figure 5.6: Mode shapes for mode numbers 21 and 25, and the corresponding natural frequencies while using C3D8 element type



(a) Mode no. 21 – Frequency = 322.178 kHz



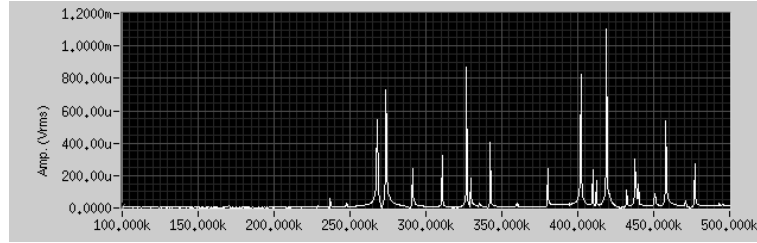
(b) Mode no. 25 – Frequency = 322.229 kHz

Figure 5.7: Mode shapes for mode numbers 21 and 25, and the corresponding natural frequencies while using C3D8R element type

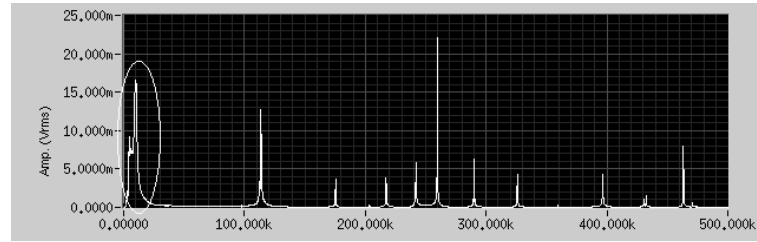
We can observe the characteristic hourglassing effect in the mode shape when reduced integration elements are used, where the model retains its shape as a whole, but individual elements look distorted. Reduced hourglassing is desired in problems where the stiffness of the individual elements should be under-estimated, for example, particularly non-linear problems such as plasticity, creep or incompressible materials.

5.2.2 Constraints on the model

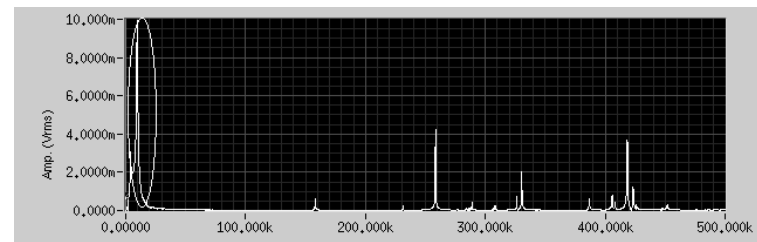
Frequency analysis under the linear perturbation module in ABAQUS gives us the free vibration modal analysis of our model. In the RUS experiment, however, there is a possibility of the existence of constraints at the points where the sample is held by the pinducers. If that is the case, those constraints need to be modeled as well in ABAQUS. The experimental results always had a few peaks in the lower frequency range that did not show up in the simulation results as expected. Figure 5.8 shows these low frequency modes in the experimental results of various samples.



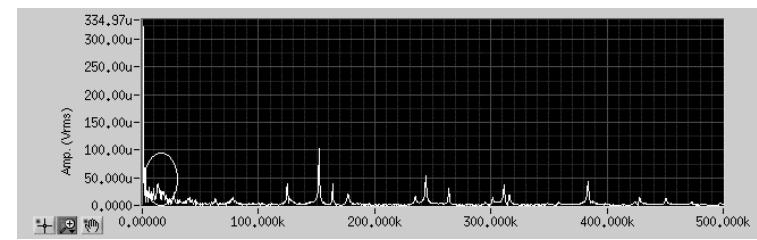
(a)



(b)



(c)



(d)

Figure 5.8: Low frequency modes (circled) for steel hex nut (b), Nb rectangular parallelepiped (c), and Nb thin disc (d).

Al parallelepiped result (a) is shown to prove that the modes occur only at a low frequency

U1, U2 and U3 constraint boundary conditions were added to opposite corners of the parallelepiped in the simulation to see if there was any improvement in the results. 16200

elements were used, with material properties same as those used in mesh type study.

Table 5.1 shows the frequency response from the experiment in the lower range of 1kHz to 20 kHz, and the first six mode results from the simulation for constrained and unconstrained models.

Table 5.1: Experimental frequency response (low frequency range) vs simulation results-constrained vs simulation results-unconstrained

Mode no.	Experiment	Simulation (constrained)	Simulation (unconstrained)
	Frequency (Hz)	Frequency (Hz)	Frequency (Hz)
1	5.018×10^3	11.885×10^{-3}	0
2	9.131×10^3	9.2674×10^3	0
3	10.418×10^3	9.6545×10^3	0
4	11.117×10^3	15.9438×10^3	0
5	14.879×10^3	18.8737×10^3	7.5393×10^{-3}
6	18.516×10^3	22.0897×10^3	13.4411×10^{-3}

It would seem that the results of the constrained FEM model match up with the experimental frequency response at low range. The full comparison is provided in table 5.5 in appendix E which shows that higher frequency modes do match between the experiment and the simulations. However, observing the mode shapes for these results proves that they are not valid modes as seen in figure 5.9. They are just rigid body modes calculated by ABAQUS causing the corner elements to be distorted similar to the hourglassing effect. The reason these low frequency modes show up in the experiment is

because of the response of the structure of the experimental setup itself which somehow the lock-in amplifier picks up as part of the natural frequency response.

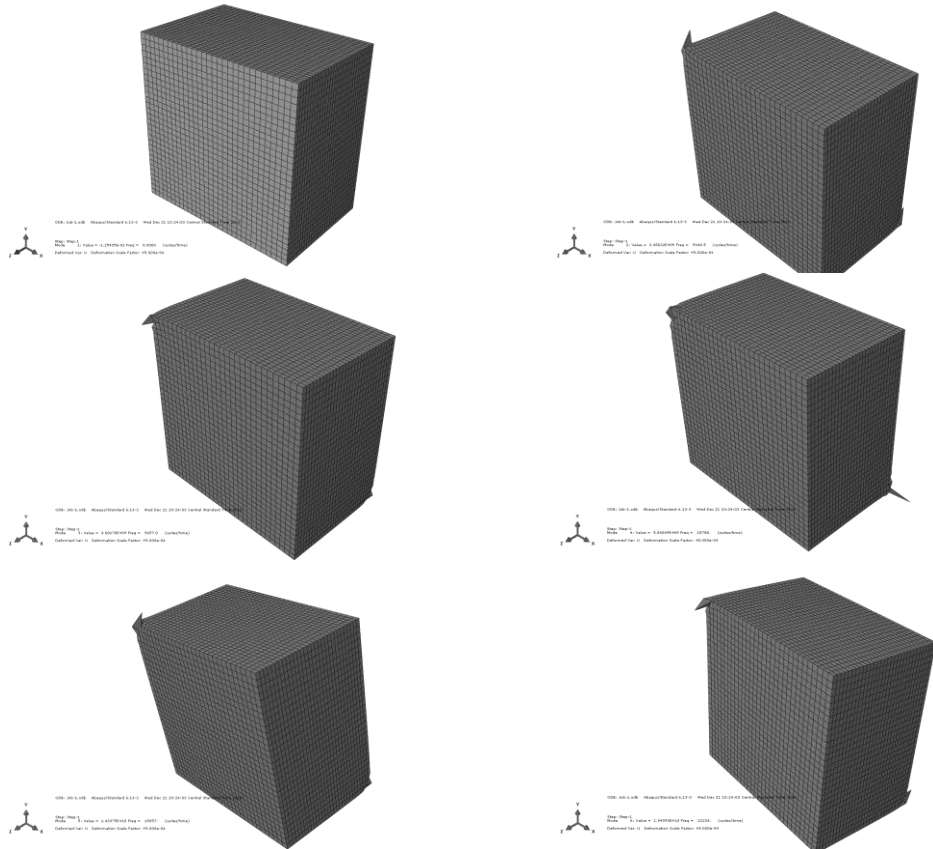


Figure 5.9: Mode shapes for the first six normal modes of free vibration in the constrained FEM model

Thus, the lower frequency range and the first six modes are not used for comparison as we can observe in the following sections that there is good agreement between experiment and simulation results in the higher frequency range.

5.2.3 Mesh fineness

To establish a minimum element count, while maintaining accuracy, a mesh fineness study was conducted where the element count was increased in large increments

and the results compared to observe the amount of error in mode frequencies. This is calculated as shown in equation 5.1.

$$error\%_n = \frac{|f_{max} - f_n|}{f_{max}} * 100 \quad 5.1$$

n represents the number of elements and max represents the highest number of elements considered. Thus f_n would be the mode frequency for n elements and f_{max} , the frequency for the highest number of elements in the study, and $error\%_n$, the percentage error of a particular mode for n elements. In this case, the different element counts are 16200, 164775, 253125 and 652864. Thus, the three different n would be 16200, 164775 and 253125, whereas max would be 652864. The element type was C3D8 with no constraints on the model. It was found that meshing it finer than approximately 700000 elements ended up in a simulation error. This is because the part geometry is small and consequently the individual element mass matrix would be too small causing an insufficient memory error.

The mode numbers considered for comparison is from mode number 7 to mode number 30. The results are shown in appendix B table 5.2. It was observed that even with 16200 elements, which drastically cuts down on the computation time, the error is below 1 % in the chosen frequency range. Figure 5.10 shows the plot of the results of the mesh fineness study. We can observe the near superimposition of data points in the plot, indicative of how low the error is between the results.

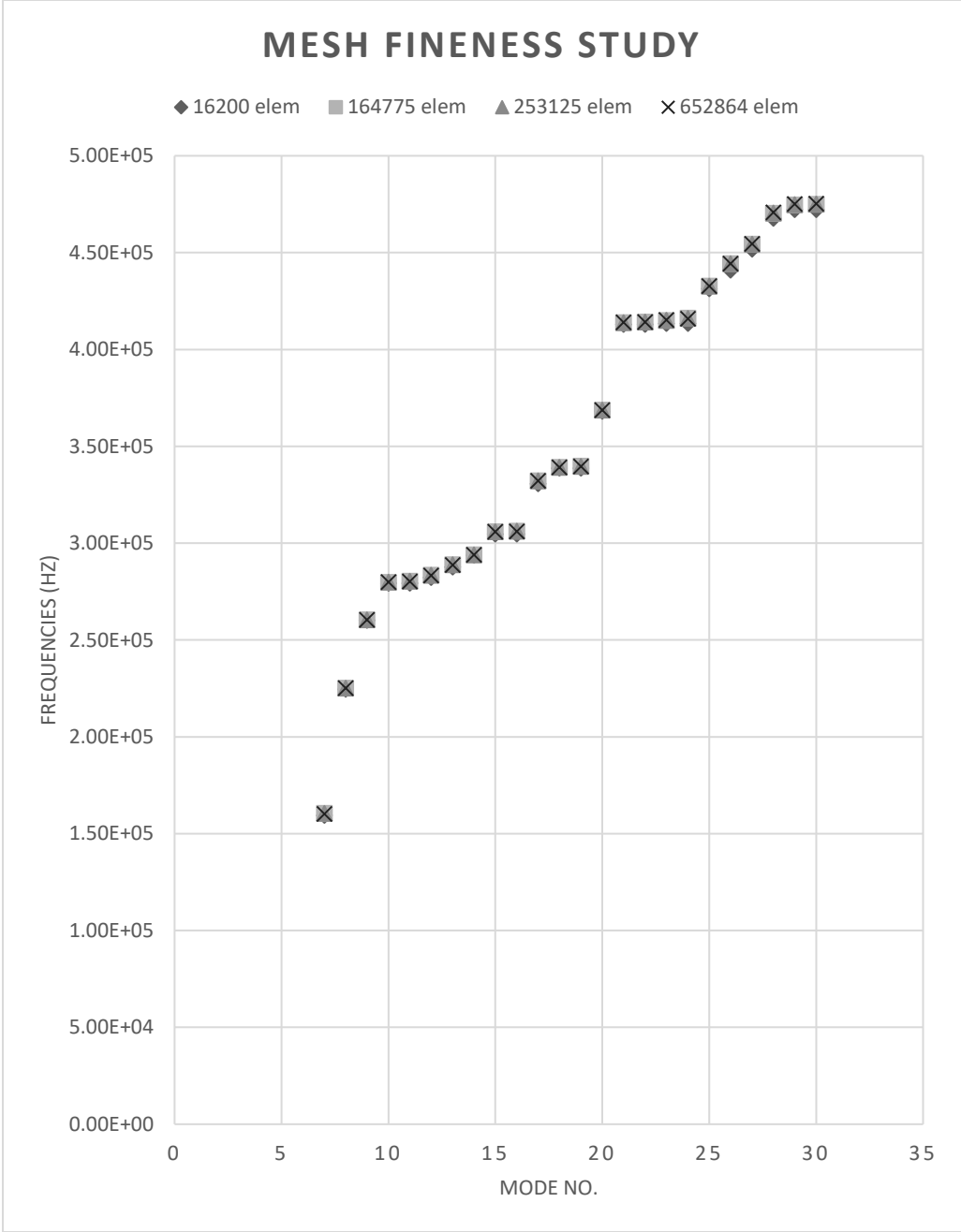


Figure 5.10: Mesh fineness study results

5.3 ABAQUS simulation: Parametric study results

The parameters varied in the simulation were Young's modulus, Poisson's ratio, and the density of the material, assuming elastic isotropy. Three different values were chosen for each parameter as shown in Table 5.3, resulting in 27 different combinations. Even though only 7 combinations are required for comparing the results and establishing a trend, the simpler method was to write the code to auto-calculate all the combinations rather than specify the values for each combination. Also, since only 16200 elements are used in the study, computation time would not be a huge deal. The element type used was C3D8 with no constraints on the model.

Table 5.3: Different material property values chosen for the parametric study.

#	Young's modulus (GPa)	Poisson's ratio	Density (kg/m ³)
1	90	0.3	8400
2	105	0.4	8570
3	120	0.5	8740

Two of the parameters are kept constant while the third one is varied. The results are obtained for each different value of the parameter that is varied. These results are converted to graphs with a simple MATLAB given in appendix C. The graphs are shown in figures 5.11 – 5.13. The corresponding data is provided in table 5.6 in appendix F.

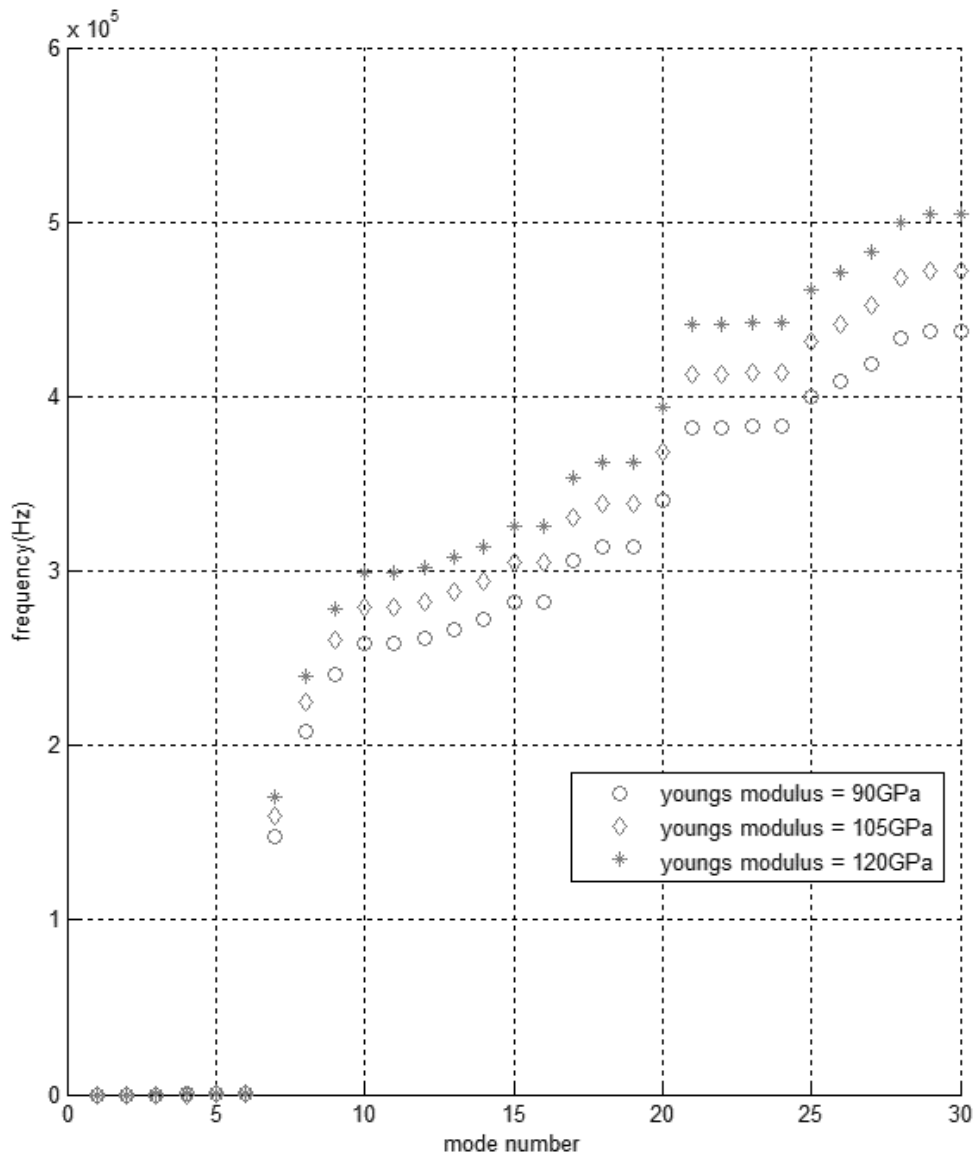


Figure 5.11: Density and Poisson's ratio kept constant, and Young's modulus is varied. Density = 8570 kg/m³,

Poisson's ratio = 0.4

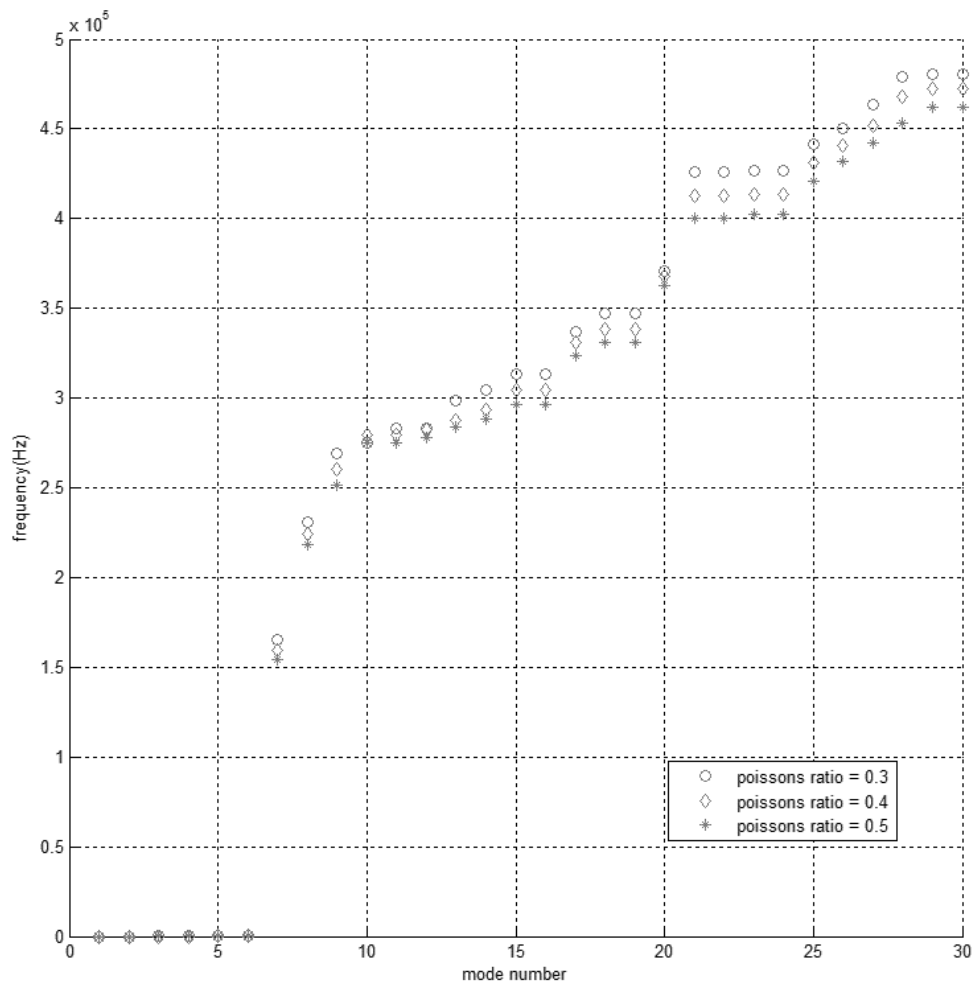


Figure 5.12: Density and Young's modulus kept constant, and Poisson's ratio is varied. Density = 8570 kg/m³, Young's modulus = 105 GPa

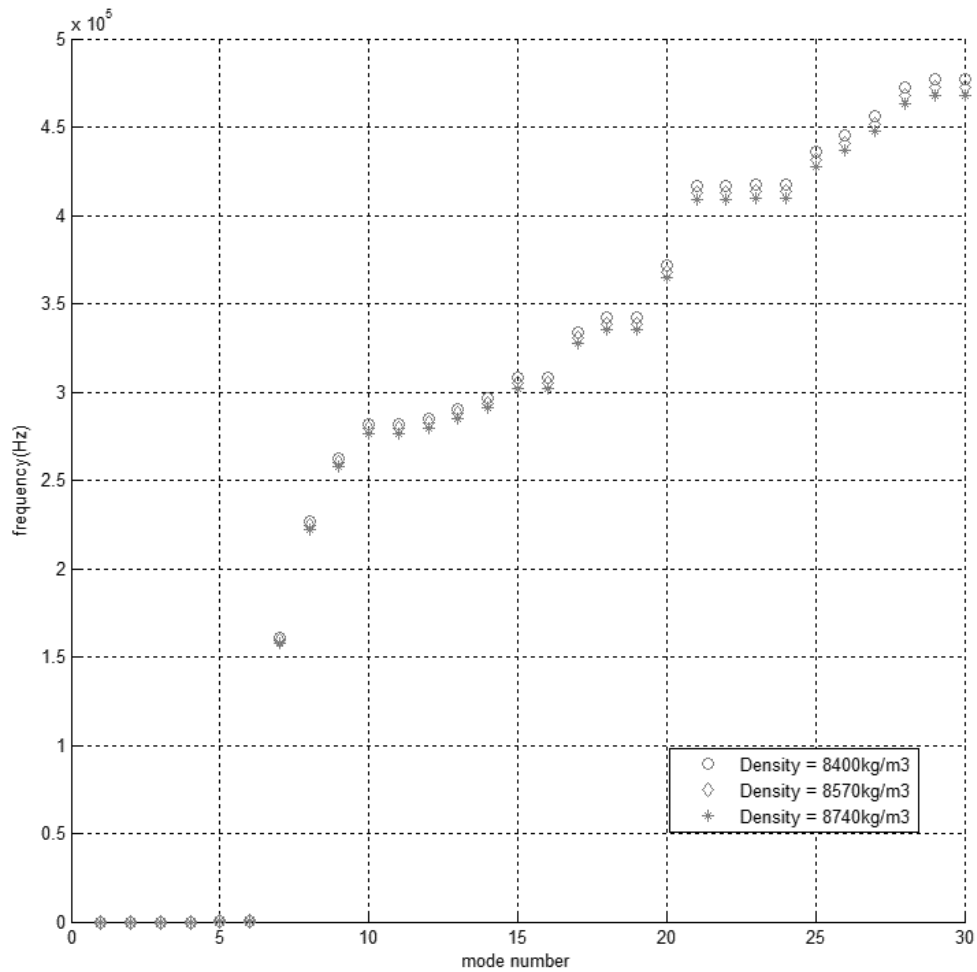
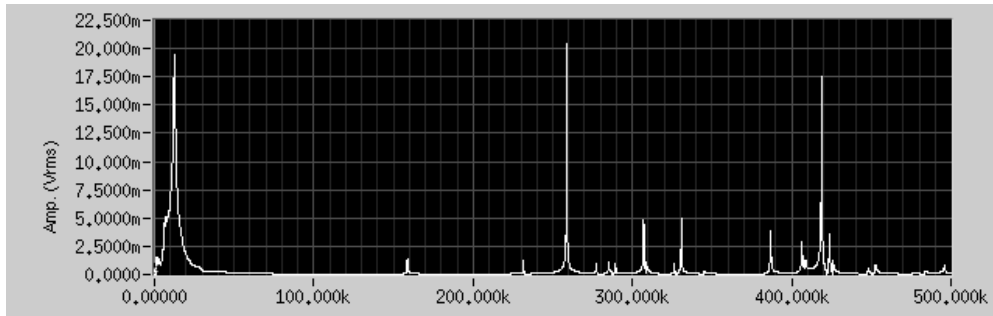


Figure 5.13: Poisson's ratio and Young's modulus kept constant, and density is varied. Poisson's ratio = 0.4, Young's modulus = 105 GPa

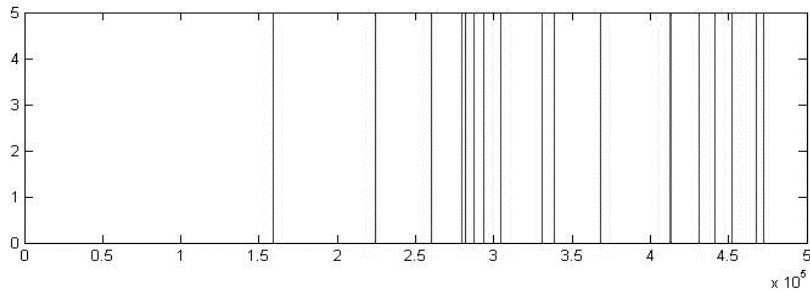
As observed in the graphs, the values of the mode frequencies shifted when one of the material properties changed. For increasing Young's modulus, the frequency shifts to a higher value whereas it is the opposite in the other two cases. It is also observed that the frequency shift is hardly noticeable for density changes compared to the shift with varying Young's modulus and Poisson's ratio. For varying Poisson's ratio, some mode numbers don't have that much of a frequency shift (for example mode numbers 10, 12 and 20). As mentioned before, results considered are for mode numbers 7 to 30.

5.4 Experimental frequency response results vs simulation results

Just for a visual comparison of the experimental and simulation results, the simulation results are converted to a simple graph (MATLAB code provided in Appendix D) with vertical lines representing mode numbers. This graph is lined up with the frequency response graph from the experiment. Figure 5.14 shows the graphical comparison for the Niobium rectangular parallelepiped with dimensions 5.03 mm x 5.03 mm x 3.2 mm. The experiment was conducted for 2000 data points. For the simulation, 16200 C3D8 type elements were used with density, Young's modulus and Poisson's ratio being 8570 kg/m³, 105 GPa and 0.4 respectively. The material property definition in the simulation was in the isotropic category, as before.



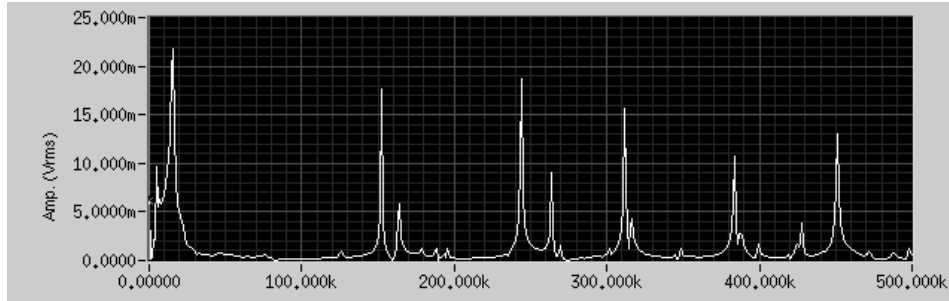
(a)



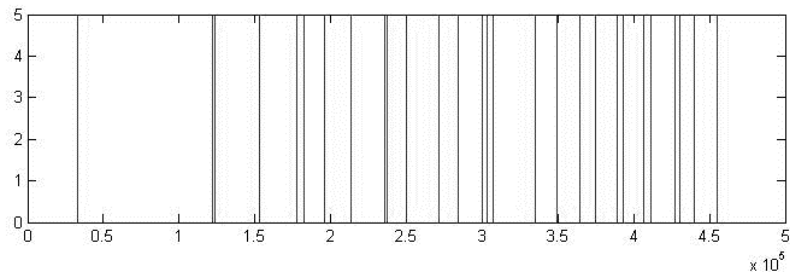
(b)

Figure 5.14: Experimental (a) vs simulation (b) results for Nb rectangular parallelepiped

This comparison is also done for a 1 mm thick Nb disc of diameter 10 mm. For the simulation, 12983 tetrahedral elements were used with isotropic material properties being same as those used in the parallelepiped simulation. The graphs are shown in figure 5.15.



(a)



(b)

Figure 5.15: Experimental (a) vs simulation (b) results for a 1 mm thick, 10 mm diameter Nb disc

The experiment and simulation was also conducted for a small hexagonal steel nut to get the comparison for a more complex geometry. Figure 5.16 shows a rough model created in ABAQUS with approximate dimensions as the actual nut. The material properties used in the simulation was that of carbon steel (Density = 7870 kg/m^3 , Young's modulus = 200 GPa, Poisson's ratio = 0.29 [24]). 18256 tetrahedral elements were used in the mesh. The graphs from experimental and simulation results are shown in figure 5.17.

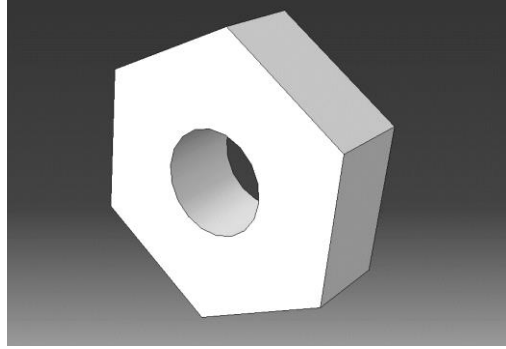
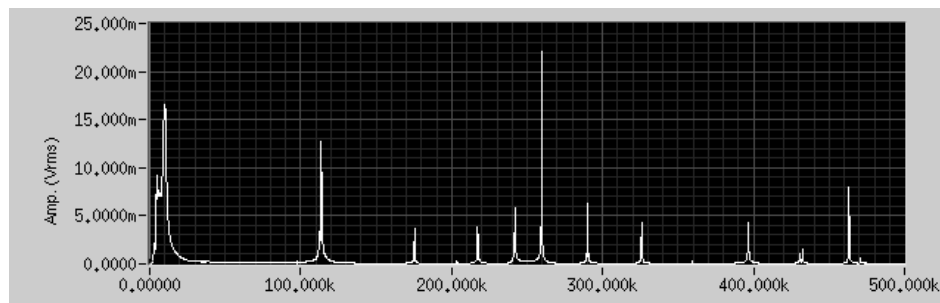
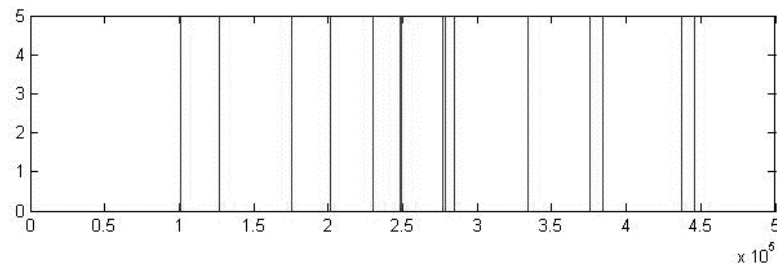


Figure 5.16: Rough model of a standard hexagonal nut created in ABAQUS



(a)



(b)

Figure 5.17: Experimental (a) vs simulation (b) results for a hexagonal steel nut

We can observe good agreement between the experimental and simulation results from these graphs for various geometries and materials. There may either be a few missing modes in the experiment or only partial matching between the experimental and the simulation results. This discrepancy is due to the uncertainty in the experimental

procedure, and the approximation involved in creating the ABAQUS model which neglects defects in the micro-structure of the material or surface imperfections.

For the detection of changes to material properties after irradiation, the natural frequency data is extracted from the data file obtained from the experiment for the Nb parallelepiped. The matching frequencies between experimental and simulation results are the ones selected to be used for comparison before and after irradiation or even for real-time monitoring. There might not be perfect matching, so an error less than 2 % could be considered acceptable. The frequency range considered is 150 kHz to 500 kHz. The simulation used 16200 C3D8 type elements and had the same isotropic material properties of Nb as used in the previous section. Table 5.4 shows the frequencies that match up with an error less than 2 % along with their experimental Q factors. Figure 5.18 shows a plot of experimental results vs simulation results.

Table 5.4: Matching frequencies between experiment and simulation of Nb rectangular parallelepiped

EXPERIMENT		SIMULATION		Error% = $\frac{ f_{\text{expt}} - f_{\text{sim}} * 100}{f_{\text{expt}}}$
Frequency (kHz) f_{expt}	Q factor	Mode no.	Frequency (kHz) f_{sim}	
160.112	2.37156	7	159.388	0.4523
228.321	2.73352	8	224.464	1.6896
259.632	527.9303	9	260.107	0.1829
282.708	1.6344	12	282.180	0.1869
287.743	1.7027	13	287.703	0.0142
291.568	2.1556	14	293.679	0.7239
306.943	0.1491	15	304.690	0.7342
328.726	160.4059	17	330.706	0.6021
332.578	362.1141	18	338.732	1.8503
411.181	9.3481	21	412.884	0.4141
420.035	260.181	23	413.431	1.5723
424.235	167.126	25	431.367	1.6810
449.850	0.4592	27	451.805	0.4345

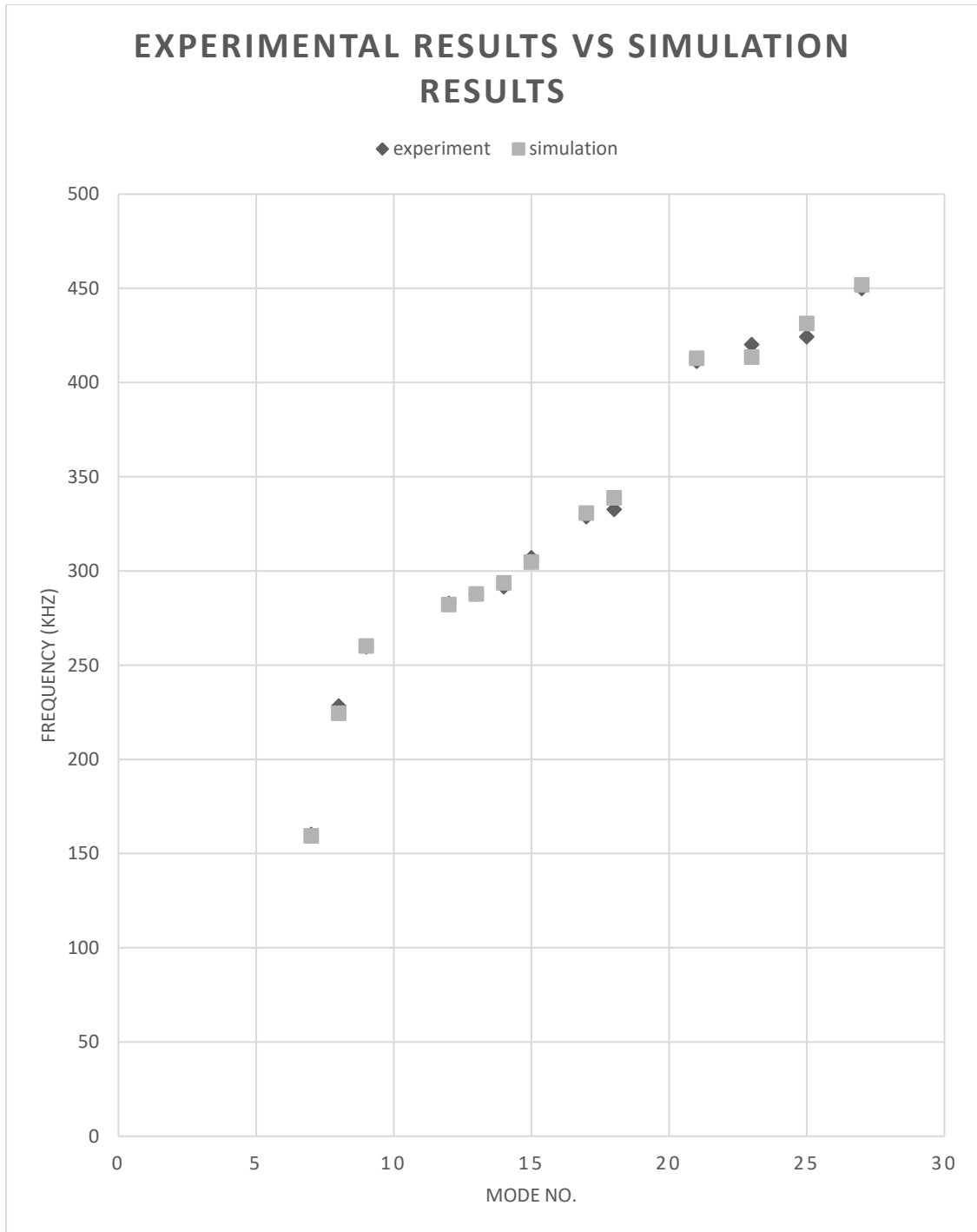


Figure 5.18: Experimental results vs simulation results. Resonance frequencies corresponding to mode numbers 10, 11, 16, 19, 20, 22, 24, 26, 28, 29 and 30 from the simulation results do not show up in the experimental frequency response.

The Q factor is inversely related to attenuation. This means that materials with low Q factor have high losses [25]. This was done on an unirradiated Nb sample since there was no access to required facilities at the time this research was conducted.

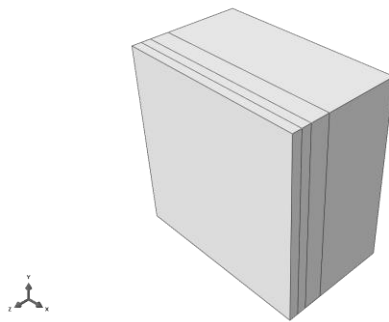
A rough radiation damage model (inhomogeneous model) was also constructed in ABAQUS with varying material properties as shown in figure 5.19. The model dimensions were 5 mm x 5 mm x 3 mm. 38400 C3D8 type elements were used in the model. For comparison, a homogeneous model was constructed with the same number of elements but with homogeneous material properties of Niobium (Young's modulus = 105 GPa, Poisson's ratio = 0.4, Density = 8570 kg/m³). The results are as shown in figure 5.20. The data is also presented in table 5.7 in appendix G. The purpose of this study was to observe the effect of inhomogeneity on the natural frequency results of the ABAQUS simulation. We can observe that there is a similar shift in the frequency results as observed in the parametric study where Young's modulus was varied.

SIDE VIEW OF THE SAMPLE
(TOTAL THICKNESS = 3 MM)

E=100 GPa, density = 8520 kg/m ³	E=95 GPa, density = 8470 kg/m ³	E=80 GPa, density = 8370 kg/m ³	E=105 GPa, density = 8570 kg/m ³
0.25 mm	0.25 mm	0.5 mm	2 mm

POISSON'S RATIO = 0.4 THROUGHOUT

(a)



(b)

Figure 5.19: Inhomogeneous model pictorial representation (a) and ABAQUS model (b)

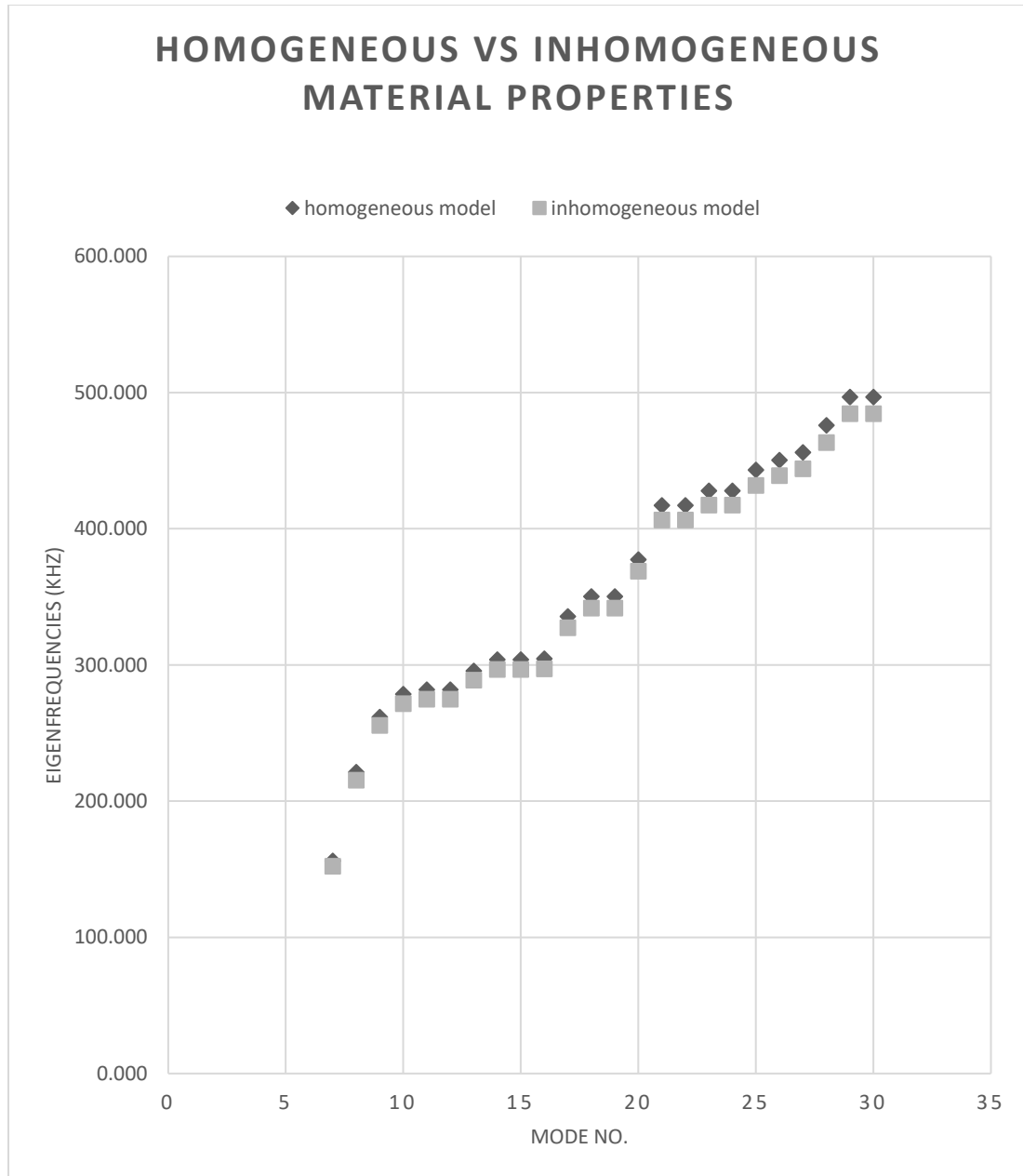


Figure 5.20: Homogeneous vs inhomogeneous material property model results

The experimental run time or update interval depends on the number of data points chosen and the sample rate chosen in the LabVIEW settings. For the given frequency range, 2000 data points gives a good resolution. The run time for each trial was about 3 minutes. For the simulation, the run time varies depending on the computational

power and surprisingly enough, the storage memory available for output files. The run time for the simulation (16200 elements) on a commercial PC with decent processor speed and RAM was about 4 minutes. This makes this process suitable for real time monitoring of a sample and detect changes in frequency response, and consequently measure changes to its elastic constants based on the trend in the frequency shift observed in the parametric study.

CHAPTER 6 – CONCLUSIONS AND FUTURE WORK

The main goal of this thesis was to observe the validity of Resonant Ultrasound Spectroscopy as a potential non-destructive evaluation technique in estimating the changes to the materials mechanical properties in a harsh radiation environment, similar to spaces surrounding an accelerator tube, where proton irradiation is quite common. This required knowledge about different types of radiation damage, and how it affects the material at a physical and mechanical level. The research itself involved conducting RUS experiments on samples of different materials and geometries, and comparing it to Finite Element simulations on ABAQUS. Actual ‘before and after irradiation’ measurements were not done due to lack of access.

6.1 Conclusions

Firstly, the repeatability of the RUS experiment was confirmed for different geometries of Niobium (Nb) by obtaining consistent results even after remounting the samples between trials. The frequency range considered was from 1 kHz to 500 kHz. The orientation of the sample with respect to the pinducers played an important role in getting good repeatable results. For rectangular parallelepipeds, only three separate trials (sample remounted between each trial) were required to get three similar results. For a hexagonal steel nut however, at least six separate trials were needed to obtain three sets of repeatable data. For the niobium discs, five trials were required to get three repeatable sets of data.

Next, the simulation results were validated by conducting a mesh study which showed that the element type and element count to be used in simulations depend on the

geometry of the sample. Reduced integration elements could not be used due to the hourglassing effect giving wrong mode frequency results. For a rectangular parallelepiped geometry, an 8-node 3D brick element gave good results, and for a disc shaped sample geometry, a 4-node tetrahedral element had to be used. It was also found that applying U1, U2 and U3 constraints to the opposite corners of the sample gave us the low frequency results that showed up in the experiment, but upon observing the mode shapes it was confirmed that they were invalid modes i.e., rigid body modes with the corner elements unusually distorted. Thus, low frequencies were no longer considered and the frequency range chosen for future comparisons was from 150 kHz to 500 kHz. In this range, results of simulations with element counts of 16200 and 652864 showed that 16200 elements can be used with an error less than 1 %.

A parametric study showed mode frequencies shifting to a higher value when Young's modulus is increased while density and Poisson's ratio is kept constant. It was the opposite for when only density and only Poisson's ratio is increased. There was also significantly lower shift in frequency for density changes, and for a few modes in the case of varying Poisson's ratio.

Good agreement was found between experimental and simulation results for various materials and geometries. 13 matching mode frequencies were identified between experimental and simulation results for an unirradiated Niobium rectangular parallelepiped in the frequency range of 150 kHz to 500 kHz. Resonance frequencies corresponding to mode numbers 10, 11, 16, 19, 20, 22, 24, 26, 28, 29 and 30 from the simulation results do not show up in the experimental frequency response.

6.2 Future work

We assume that the material property changes are uniform throughout the material or at least that the changes to their elastic properties behave in that manner for initial analysis. Even though a rough inhomogeneous model was analyzed, creating a more complex ABAQUS model with user defined material properties is something to consider. If the experiment is conducted on an irradiated sample, that would give us actual proof of validity of some of the assumptions and theories in this research. RUS can also potentially be used to detect changes in geometries of assembled samples by studying the amplitude responses if proper repeatability is achieved. It is also worth exploring the possibility of modifying the pinducers to get a sharper tip for better point contact with the sample to see if it influences the experimental results in any way.

REFERENCES

- [1] J. Maynard, "Resonant Ultrasound Spectroscopy," *Physics today*, pp. 26-31, 1996.
- [2] A. T. R. W.M.Visscher, "On the normal modes of free vibration of inhomogenous and anisotropic elastic objects," *Journal of Acoustical Society of America*, vol. 90, pp. 2154-2162, 1991.
- [3] R. Eriksson, "European Spallation Source," ESS, [Online]. Available: <https://europeanspallationsource.se/spoke-srf>. [Accessed 5 October 2015].
- [4] A. R. M. Iasir, "Developing a Non-Destructive Evaluation Technique Using Resonant Ultrasound Spectroscopy for Fission Based Target," University of Missouri, Columbia, 2015.
- [5] G. J. Dienes, "Radiation effects in solids," *Annual Review of Nuclear Science*, no. 2.1, pp. 187-220, 1953.
- [6] K. L. N. ., a. W. H. W. Z. Wang, "Understanding the changes in ductility and Poisson's ratio of metallic glasses during annealing from microscopic dynamics," American Institute of Physics, 2015.
- [7] M. Izerroukenn, "Radiation damage induced in Zircaloy-4 by 2.6 MeV proton irradiation," *Journal of radioanalytical and nuclear chemistry*, vol. 311, no. 3, pp. 1917-1921, 2017.
- [8] G.S.Was, *Fundamentals of Radiation Materials Science*, Berlin: Springer, 2007.

- [9] "International Atomic Energy Agency," 22 August 2007. [Online]. Available: https://www.iaea.org/About/Policy/GC/GC51/GC51InfDocuments/English/gc51inf-3-att7_en.pdf. [Accessed 10 March 2017].
- [10] N. Budylnin, "Neutron-induced swelling and embrittlement of pure iron and pure nickel irradiated in the BN-350 and BOR-60 fast reactors," *Journal of Nuclear Materials*, no. 375, pp. 359-364, 2008.
- [11] A. S. H. Dieckamp, "Effect of Electron Irradiation on Young's Modulus," *Journal of Applied Physics*, no. 27.12, pp. 1416-1418, 1956.
- [12] X. G. X. S. H. H. G. L. D.-Y. Zhu, "Effects of vacancies on the mechanical properties of zirconium: An ab initio investigation," *Materials and design*, vol. 119, pp. 30-37, 2017.
- [13] J. Guoxing Liu, "Measuring elastic constants of arbitrarily shaped samples using resonant ultrasound spectroscopy," *Journal of Acoustical Society of America*, vol. 131, pp. 2068-2078, 2012.
- [14] H. Ekstein, "Free Vibrations of Isotropic Cubes and Nearly Cubic Parallelepipeds," *Journal of applied physics*, vol. 27, no. 4, pp. 405-412, 1956.
- [15] A. F. Bower, "Applied Mechanics of Solids," 2008. [Online]. Available: http://solidmechanics.org/text/Chapter3_2/Chapter3_2.htm. [Accessed 10 March 2017].
- [16] M. a. Spoor, "Elastic isotropy and anisotropy in quasicrystalline and cubic AlCuLi,"

Phys. Rev. Lett., pp. 3462-3465, 1995.

- [17] R. K. Bollinger, B. D. White, J. J. Neumeier, H. R. Z. Sandim, Y. Suzuki, C. A. M. dos Santos, R. Avci, A. Migliori and J. B. Betts, "Observation of a Martensitic Structural Distortion in V, Nb, and Ta," *American Physical Society*, vol. 107, no. 7, 2011.
- [18] A. Yoneda, "Pressure derivatives of elastic constants of single crystal MgO and MgAl₂O₄," *Journal of Physics of the Earth*, no. 38.1, pp. 19-55, 1990.
- [19] Leighton-Watson, "Github," [Online]. Available:
<https://github.com/PALab/RUS/tree/master/Fitspectra>. [Accessed 5 January 2017].
- [20] T. J. Hughes, "The finite element method: linear static and dynamic finite element analysis," *Courier Corporation*, p. 582, 2012.
- [21] Simulia, Getting started with ABAQUS, ABAQUS documentation.
- [22] E. Biedermann, "Uncertainty quantification in modeling and measuring components with resonant ultrasound spectroscopy," in *AIP Conference Proceedings*, 2016.
- [23] "WebElements," [Online]. Available:
<https://www.webelements.com/niobium/physics.html>. [Accessed 5 October 2015].
- [24] "Carbon Steel Mechanical Properties," Ezlok, [Online]. Available:
<https://www.ezlok.com/TechnicalInfo/MPCarbonSteel.html>. [Accessed 19 September 2016].

[25] A. L. S. J. Migliori, Resonant ultrasound spectroscopy: applications to physics, materials measurements, and nondestructive evaluation., Wiley-Interscience, 1997.

APPENDIX A

Python code for parametric study:

```
#create study
nb=ParStudy(par=('nu','E','ro'))
#parameter definition
nb.define(CONTINUOUS,par='nu',domain=(.3,.5))
nb.define(CONTINUOUS,par='E',domain=(90e9,120e9))
nb.define(CONTINUOUS,par='ro',domain=(8400,8740))
#parameter sampling
nb.sample(NUMBER,par='nu',number=3)
nb.sample(NUMBER,par='E',number=3)
nb.sample(NUMBER,par='ro',number=3)
#sample combination
nb.combine(MESH,name='partest')
#generate analysis job data
nb.generate(template='pse')
#job execution
nb.execute(ALL)
```

APPENDIX B

Table 5.2: Mesh fineness study comparison

mode no.	16200elem frequency(Hz)	164775elem frequency(Hz)	253125elem frequency(Hz)	652864elem Frequency(Hz)	16200 Err%	164775 Err%	253125 Err%
7	1.59E+05	1.61E+05	1.60E+05	1.60E+05	5.22E-01	2.17E-01	1.39E-01
8	2.24E+05	2.25E+05	2.25E+05	2.25E+05	2.95E-01	8.00E-03	3.55E-03
9	2.60E+05	2.60E+05	2.60E+05	2.60E+05	9.03E-02	5.07E-02	3.26E-02
10	2.79E+05	2.80E+05	2.80E+05	2.80E+05	1.97E-01	2.47E-02	1.39E-02
11	2.79E+05	2.80E+05	2.80E+05	2.80E+05	3.44E-01	5.35E-02	3.60E-02
12	2.82E+05	2.83E+05	2.83E+05	2.83E+05	4.10E-01	5.51E-02	3.67E-02
13	2.88E+05	2.89E+05	2.89E+05	2.89E+05	3.61E-01	6.75E-02	4.36E-02
14	2.94E+05	2.94E+05	2.94E+05	2.94E+05	1.20E-01	1.63E-02	9.52E-03
15	3.05E+05	3.06E+05	3.06E+05	3.06E+05	3.85E-01	1.21E-02	9.81E-03
16	3.05E+05	3.06E+05	3.06E+05	3.06E+05	4.53E-01	5.46E-02	3.69E-02
17	3.31E+05	3.32E+05	3.32E+05	3.32E+05	4.49E-01	1.44E-02	6.02E-03
18	3.39E+05	3.39E+05	3.39E+05	3.39E+05	1.36E-01	1.09E-02	6.19E-03
19	3.39E+05	3.40E+05	3.40E+05	3.40E+05	2.45E-01	5.42E-02	3.56E-02
20	3.68E+05	3.69E+05	3.69E+05	3.69E+05	1.41E-01	7.05E-03	3.80E-03
21	4.13E+05	4.14E+05	4.14E+05	4.14E+05	2.55E-01	2.75E-02	1.57E-02
22	4.13E+05	4.14E+05	4.14E+05	4.14E+05	2.97E-01	3.14E-03	2.41E-04
23	4.13E+05	4.15E+05	4.15E+05	4.15E+05	4.25E-01	4.43E-02	2.53E-02
24	4.13E+05	4.16E+05	4.16E+05	4.16E+05	5.91E-01	5.24E-02	3.61E-02
25	4.31E+05	4.33E+05	4.33E+05	4.33E+05	3.00E-01	1.29E-02	9.94E-03
26	4.41E+05	4.44E+05	4.44E+05	4.44E+05	7.58E-01	5.18E-03	1.13E-03
27	4.52E+05	4.54E+05	4.54E+05	4.55E+05	5.97E-01	3.76E-02	1.98E-02
28	4.68E+05	4.70E+05	4.71E+05	4.71E+05	6.55E-01	8.67E-02	5.03E-02
29	4.72E+05	4.75E+05	4.75E+05	4.75E+05	6.09E-01	8.48E-02	4.99E-02
30	4.72E+05	4.75E+05	4.75E+05	4.75E+05	6.46E-01	6.21E-02	3.56E-02

APPENDIX C

MATLAB code for obtaining parametric study trend graphs:

```
%Create y axis data set%
y=[1:30];
hold on;
%c11,c14 and c17 are rows of data imported from rpt files%
%Update as new data is imported%
plot(y',c11,'ro');
plot(y',c14,'rd');
plot(y',c17,'r*');
hold off;
xlabel('mode number');
ylabel('frequency(Hz)');
grid on;
%Legend is updated for different cases%
legend('youngs modulus = 90GPa','youngs modulus = 105GPa','youngs
modulus = 120GPa');
```

APPENDIX D

MATLAB code for creating simple graphs of simulation results:

```
%create y axis data%
y=zeros(500000,1);
%c14 is the imported data from rpt file. Update if necessary%
a=c14(:,2);
%create x axis data%
x=1:500000;
for j=1:30
    for i=1:500000
        if i==a(j)
            y(i)=5;
        end
    end
end
end
plot(x,y)
```

APPENDIX E

Table 5.5: Constrained model vs unconstrained model – full comparison

Mode no.	Experiment	Simulation (constrained)	Simulation (unconstrained)
	Frequency (Hz)	Frequency (Hz)	Frequency (Hz)
1	5.018×10^3	11.885×10^3	0
2	9.131×10^3	9.2674×10^3	0
3	10.418×10^3	9.6545×10^3	0
4	11.117×10^3	15.9438×10^3	0
5	14.879×10^3	18.8737×10^3	7.5393×10^3
6	18.516×10^3	22.0897×10^3	13.4411×10^3
7	160.112×10^3	158.897×10^3	160.878×10^3
8	228.321×10^3	224.084×10^3	226.67×10^3
9	259.632×10^3	261.759×10^3	261.655×10^3
10	-	281.613×10^3	281.219×10^3
11	-	281.771×10^3	281.219×10^3
12	282.708×10^3	282.123×10^3	285.011×10^3
13	287.743×10^3	295.633×10^3	288.308×10^3
14	291.568×10^3	296.450×10^3	295.633×10^3
15	306.943×10^3	306.006×10^3	307.259×10^3
16	-	306.162×10^3	307.259×10^3
17	328.726×10^3	334.455×10^3	333.059×10^3
18	332.578×10^3	345.041×10^3	340.205×10^3
19	-	345.159×10^3	340.205×10^3
20	-	373.849×10^3	369.948×10^3
21	411.181×10^3	416.477×10^3	415.704×10^3
22	-	416.535×10^3	415.704×10^3
23	420.035×10^3	421.807×10^3	415.838×10^3
24	-	422.023×10^3	415.838×10^3
25	424.235×10^3	438.610×10^3	433.71×10^3
26	-	450.192×10^3	444.121×10^3
27	449.850×10^3	453.768×10^3	456.44×10^3
28	-	158.897×10^3	471.6×10^3

29	-	224.084×10^3	474.744×10^3
30	-	261.759×10^3	474.744×10^3

APPENDIX F

Table 5.6: Parametric study data

Mode no.	Young's modulus varied (Density = 8570 kg/m ³ , Poisson's ratio = 0.4)		
	Young's modulus = 90 GPa Eigenfrequencies (kHz)	Young's modulus = 105 GPa Eigenfrequencies (kHz)	Young's modulus = 120 GPa Eigenfrequencies (kHz)
1	0	0	0
2	0	0	0
3	0	0	3.83964E-06
4	8.47683E-06	0	1.92152E-05
5	1.49766E-05	7.53929E-06	2.39161E-05
6	1.89918E-05	1.34411E-05	2.78203E-05
7	147.564	159.388	170.392
8	207.814	224.464	239.962
9	240.812	260.107	278.066
10	258.596	279.315	298.601
11	258.596	279.315	298.601
12	261.248	282.18	301.663
13	266.362	287.703	307.568
14	271.894	293.679	313.956
15	282.088	304.69	325.727
16	282.088	304.69	325.727
17	306.174	330.706	353.54
18	313.605	338.732	362.12
19	313.605	338.732	362.12
20	340.821	368.129	393.547
21	382.256	412.884	441.391
22	382.256	412.884	441.391
23	382.763	413.431	441.976
24	382.763	413.431	441.976
25	399.369	431.367	461.151
26	408.279	440.992	471.44
27	418.29	451.805	483

28	432.994	467.687	499.978
29	437.158	472.185	504.786
30	437.158	472.185	504.786
	Poisson's ratio varied (E = 105 GPa, Density = 8570 kg/m ³)		
	Poisson's ratio = 0.3 Eigenfrequencies (kHz)	Poisson's ratio = 0.4 Eigenfrequencies (kHz)	Poisson's ratio = 0.5 Eigenfrequencies (kHz)
1	0	0	0
2	0	0	0
3	4.53412E-06	0	0.00281538
4	1.42457E-05	0	0.00726234
5	1.77529E-05	7.53929E-06	0.0103722
6	2.22696E-05	1.34411E-05	0.0127163
7	165.385	159.388	154.001
8	231.036	224.464	218.436
9	269.258	260.107	251.804
10	275.284	279.315	274.786
11	283.487	279.315	274.786
12	283.487	282.18	278.076
13	298.407	287.703	283.722
14	304.763	293.679	288.611
15	312.97	304.69	296.634
16	312.97	304.69	296.634
17	336.991	330.706	323.828
18	346.985	338.732	331.198
19	346.985	338.732	331.198
20	370.958	368.129	362.493
21	425.954	412.884	400.163
22	425.954	412.884	400.163
23	426.668	413.431	402.245
24	426.668	413.431	402.245
25	441.725	431.367	421.169
26	450.514	440.992	431.861
27	463.237	451.805	442.187
28	478.692	467.687	453.224

29	480.759	472.185	462.386
30	480.759	472.185	462.386
	Density is varied (E = 105 GPa, Poisson's ratio = 0.4)		
	Density = 8400 kg/m ³ Eigenfrequencies (kHz)	Density = 8570 kg/m ³ Eigenfrequencies (kHz)	Density = 8740 kg/m ³ Eigenfrequencies (kHz)
1	0	0	0
2	0	0	0
3	0	0	0
4	0	0	0
5	7.61525E-06	7.53929E-06	7.46562E-06
6	1.35765E-05	1.34411E-05	1.33098E-05
7	160.992	159.388	157.83
8	226.724	224.464	222.271
9	262.725	260.107	257.564
10	282.128	279.315	276.586
11	282.128	279.315	276.586
12	285.021	282.18	279.422
13	290.6	287.703	284.892
14	296.636	293.679	290.809
15	307.758	304.69	301.712
16	307.758	304.69	301.712
17	334.036	330.706	327.474
18	342.143	338.732	335.422
19	342.143	338.732	335.422
20	371.836	368.129	364.531
21	417.041	412.884	408.849
22	417.041	412.884	408.849
23	417.593	413.431	409.39
24	417.593	413.431	409.39
25	435.711	431.367	427.152
26	445.432	440.992	436.682
27	456.354	451.805	447.389
28	472.395	467.687	463.116
29	476.939	472.185	467.57

30	0	472.185	467.57
----	---	---------	--------

APPENDIX G

Table 5.7: Homogeneous vs inhomogeneous model results

Mode no.	Eigenfrequencies (kHz)	
	Homogeneous model	Inhomogeneous model
7	156.188	152.250
8	221.190	215.436
9	261.704	255.490
10	278.471	271.532
11	281.926	274.856
12	281.926	274.856
13	295.612	288.758
14	303.980	296.601
15	303.980	296.601
16	304.500	297.110
17	335.569	327.382
18	350.164	341.673
19	350.164	341.673
20	377.453	368.789
21	417.089	406.512
22	417.089	406.512
23	427.928	417.310
24	427.928	417.310
25	443.114	431.814
26	450.446	439.062
27	456.039	444.058
28	475.881	463.335
29	496.818	484.494
30	496.818	484.494